


Simulation of Linear Non-Hermitian Boundary-Value Problems with Quantum Singular-Value Transformation

I. Novikau^{1,*}, I.Y. Dodin^{1,2} and E.A. Startsev¹

¹*Princeton Plasma Physics Laboratory, Princeton, New Jersey 08543, USA*

²*Department of Astrophysical Sciences, Princeton University, Princeton, New Jersey 08544, USA*

 (Received 18 December 2022; revised 12 March 2023; accepted 29 March 2023; published 3 May 2023)

We propose a quantum algorithm for simulating dissipative waves in inhomogeneous linear media as a boundary-value problem. Using the so-called quantum singular value transformation (QSVT), we construct a quantum circuit that models the propagation of electromagnetic waves in a one-dimensional system with outgoing boundary conditions. The corresponding measurement procedure is also discussed. Limitations of the QSVT algorithm are identified in connection with the large condition numbers that the dispersion matrices exhibit at weak dissipation.

DOI: [10.1103/PhysRevApplied.19.054012](https://doi.org/10.1103/PhysRevApplied.19.054012)

I. INTRODUCTION

First-principle (“full-wave”) modeling of linear waves in inhomogeneous linear media is fundamental for various applications, for example, plasma heating in fusion research [1–3]. However, it can be computationally expensive, especially for waves with wavelengths that are orders magnitude smaller than the characteristic inhomogeneity scales. Such simulations can be facilitated by quantum computing (QC).

Here, we focus on potential applications of future noiseless error-corrected gate-based quantum computers. For such computers, quantum algorithms have been proposed for initial-value problems that involve purely Hermitian interactions, such as the propagation of electromagnetic (EM) waves in cold magnetized plasma [4] and also Landau damping of kinetic plasma waves [5]. However, practical applications are usually concerned with dissipative waves and are set up as boundary-value problems, also called antenna problems. The corresponding codes (Refs. [6–8], to name a few) are often used to model EM waves in fusion plasmas [9–11]. After discretization, such problems can be represented as linear vector equations of the form

$$A\psi = b, \quad (1)$$

where A of size $N \times N$ is generally a non-Hermitian invertible matrix, b is a given vector, and the vector ψ represents the field(s) of interest [12].

The first quantum method to solve Eq. (1), the so-called Harrow-Hassidim-Lloyd (HHL) algorithm, was presented in Ref. [13]. This method was developed further in

Refs. [14,15], where its scaling with the condition number κ of the matrix A and the absolute error has been improved. A thorough analysis of the HHL algorithm in application to EM classical-wave problems was given in Ref. [16]. It was demonstrated there that the time necessary for a single run of the corresponding HHL circuit to achieve quantum advantage is comparable with the age of the Universe (even without taking into account the costs of encoding the matrix A into a quantum circuit). Hence, a concern has emerged to what extent quantum algorithms are actually applicable to boundary-value wave problems.

Here, we address this matter by developing a different approach to solving Eq. (1) on a quantum computer, namely, by using so-called quantum signal processing (QSP). Although originally developed [17,18] for Hermitian matrices, the QSP has been recently extended to general matrices using the quantum singular value transformation (QSVT) [19,20]. The QSVT provides a near-optimal dependence of the query complexity (the number of calls to the subcircuit encoding A) on both the condition number and the error, so it is considered as a promising algorithm for solving linear equations.

We consider an EM wave propagating in an inhomogeneous one-dimensional dielectric medium with a source and outgoing boundary conditions. In the first part of our work, we construct a quantum circuit for the corresponding matrix A using the QSVT, emulate quantum simulations on a classical computer, and benchmark our results against those of conventional classical simulations. The second part of the work is concerned with extracting classical information from quantum circuits using measurements. In general, this step is computationally expensive, so including it is necessary when assessing the efficiency of quantum simulations [21]. We discuss how to perform

*inovikau@pppl.gov

relevant measurements in the wave problem and estimate the necessary resources. Our finding is that even with the measurement costs included, the overall quantum simulations of dissipative waves based on the QSVT scale favorably compared to classical simulations in multidimensional systems. We expect the gain to be particularly efficient in kinetic plasma problems, where the wave modeling is done in phase space with six or even more dimensions.

Our paper is organized as follows. In Sec. II, we briefly describe the QSVT algorithm and the corresponding circuit. The QSVT scaling and its comparison with classical methods are discussed in Sec. III. In Sec. IV, we outline our one-dimensional wave system and describe its discretization. The encoding of the system into a quantum circuit is discussed in detail in Sec. V. The classical modeling of the system and its quantum simulation on a digital emulator of quantum circuits are compared in Sec. VI. There, we explore circuits for basic measurements of the wave-number spectrum and the wave energy. Besides, an algorithm is proposed to measure wave absorption power, where the QSVT is used for both EM field computations and emulation of the electrical conductivity. The efficiency of the QSVT algorithm for simulations of classical waves and the related challenges that remain are discussed in Sec. VII. Auxiliary information and technical details are also discussed in Appendices A and B.

II. QUANTUM SINGULAR VALUE TRANSFORMATION

A. General idea

One of the ways to solve Eq. (1) is by calculating the inverse of the matrix A . The polynomial approximation $P_{\text{inv}}(A)$ of this function with a Hermitian A can be found on a quantum computer by using the QSP [17,18]. To compute $P_{\text{inv}}(A)$ of a non-Hermitian A , one can dilate the matrix to make it Hermitian and then use the QSP. Another possibility, which does not require the dilation, is to apply the QSVT [19,20]. The idea of this approach is based on a generalization of the classical singular value transformation

$$A = U_L S U_R^\dagger, \quad (2)$$

where $S = \text{diag}(s_1, \dots, s_N)$ is a diagonal $N \times N$ matrix with real non-negative (or strictly positive, if A is invertible) diagonal elements s_i called singular values of A ; also, U_L and U_R are complex unitary matrices. The QSVT operates with a matrix polynomial

$$P_{\text{QSVT}}(A) = U_L p(S) U_R^\dagger, \quad (3)$$

where $p(S) = \text{diag}[p(s_1), \dots, p(s_N)]$, and $p(s_i)$ is a complex polynomial of a scalar s_i . In particular, let us consider

the case when P_f is a polynomial approximation of some given function f . If A is Hermitian, then $U_L = U_R$ and, clearly, $P_{\text{QSVT}}(A) = P_f(A)$. If A is not Hermitian, then $P_{\text{QSVT}}(A)$ generally does not coincide with $P_f(A)$, but it still can be used to approximate $P_f(A)$ if f is the inverse function. This is seen as follows.

First, note that the QSVT allows one to find the Moore-Penrose pseudoinverse A^+ (which must not be confused with the Hermitian adjoint A^\dagger). From the definition of A^+ , and assuming that $A^\dagger A$ is invertible, one has $A^+ = (A^\dagger A)^{-1} A^\dagger$, so, by Eq. (2), one finds

$$A^+ = U_R S^{-1} U_L^\dagger. \quad (4)$$

Now, let us consider P_{QSVT} specifically with $p(s) \simeq s^{-1}$, where the symbol \simeq denotes a polynomial approximation. By Eq. (3), one has $P_{\text{QSVT}}(A^\dagger) = U_R S^{-1} U_L^\dagger$, and by comparing this with Eq. (4), one finds that $A^+ = P_{\text{QSVT}}(A^\dagger)$. If the matrix A is invertible, then $A^+ = A^{-1}$ and therefore one has

$$A^{-1} = P_{\text{QSVT}}(A^\dagger). \quad (5)$$

This shows that A^{-1} can be approximated with a QSVT polynomial constructed for $p(s) \simeq s^{-1}$.

B. Block encoding

Because a quantum circuit can implement only unitary operations, to decompose a matrix polynomial of a given nonunitary matrix A , one first needs to encode it as a sub-block of an auxiliary unitary U_A . This procedure is called block encoding and involves introducing additional ancilla qubits. Specifically, U_A acts as A when the ancillae are in the zero state, $|0\rangle_a$, so U_A has a form

$$U_A = \begin{pmatrix} A & \cdot \\ \cdot & \cdot \end{pmatrix}. \quad (6)$$

For this, A must be normalized such that $\zeta \|A\|_{\max} \leq 1$, where

$$\|A\|_{\max} = \max_k \sum_j \sqrt{|A_{kj}|^2}, \quad (7)$$

and ζ is related to the matrix sparsity as detailed in Sec. VC. (We define the sparsity as the number of nonzero matrix elements in a row maximized over all rows.) Otherwise, A should be renormalized as follows:

$$A \rightarrow A / (\|A\|_{\max} \zeta). \quad (8)$$

C. Polynomials via matrix rotations

The sets of right and left singular vectors u_r and u_l , which are columns of the matrices U_L and U_R , correspondingly, form two orthogonal sets. Any other vector can be

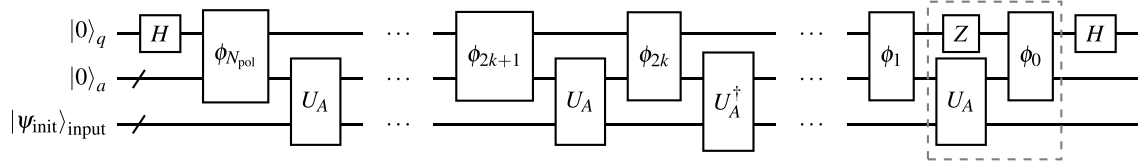


FIG. 1. Schematic of the QSVT circuit encoding a matrix real polynomial of order N_{pol} , where N_{pol} is odd, by using $N_{\text{pol}} + 1$ angles. For encoding a polynomial with even N_{pol} , the gates in the dashed box should be removed. The circuit structure is described by Eq. (13). The Pauli Z and Hadamard gates are introduced to extract the real part of the QSVT polynomial [22]. The gate U_A is the block-encoding oracle described in Sec. II B. The gates denoted as ϕ_k represent the controlled rotations $\exp(i\phi_k Z_{\Pi})$ shown in Fig. 2. The upper (lower) qubit is the most (least) significant one. The ancilla qubits a and q are initialized in the zero state, $|0\rangle_a$ and $|0\rangle_q$, respectively. The “input” register is initialized with the state $|\psi_{\text{init}}\rangle$ to be modified by the QSVT polynomial.

represented as a linear superposition of the vectors from one of these sets. Therefore, to construct U_A , it is sufficient to define the action of this operator on the vectors u_r and u_l . Assuming that u_r and u_l are associated with a given singular value s , one obtains from Eq. (2) that

$$U_A |0\rangle_a |u_r\rangle = s |0\rangle_a |u_l\rangle + \sqrt{1-s^2} |\perp_l\rangle, \quad (9a)$$

$$U_A^\dagger |0\rangle_a |u_l\rangle = s |0\rangle_a |u_r\rangle + \sqrt{1-s^2} |\perp_r\rangle, \quad (9b)$$

where $|\perp_l\rangle$ and $|\perp_r\rangle$ are vectors orthogonal to the subspace that corresponds to the ancillae a being in the zero state. Using that $U_A^\dagger U_A = 1$, one obtains

$$U_A |\perp_r\rangle = \sqrt{1-s^2} |0\rangle_a |u_l\rangle - s |\perp_l\rangle, \quad (10a)$$

$$U_A^\dagger |\perp_l\rangle = \sqrt{1-s^2} |0\rangle_a |u_r\rangle - s |\perp_r\rangle. \quad (10b)$$

The above equations indicate that U_A maps the Hilbert space spanned by $|0\rangle_a |u_r\rangle$ and $|\perp_r\rangle$ to the space spanned by $|0\rangle_a |u_l\rangle$ and $|\perp_l\rangle$. Likewise, U_A^\dagger maps $|0\rangle_a |u_l\rangle$ and $|\perp_l\rangle$ back to $|0\rangle_a |u_r\rangle$ and $|\perp_r\rangle$. Note that all these spaces remain invariant under the action of the projector Π :

$$\Pi = \begin{pmatrix} 1 & 0 \\ 0 & 0 \end{pmatrix}. \quad (11)$$

This property also extends to any function of Π . In particular, the reflector $Z_{\Pi} = 2\Pi - 1$ maps $|0\rangle_a |u_{r,l}\rangle$ to $|0\rangle_a |u_{r,l}\rangle$, and $|\perp_{r,l}\rangle$ to $-|\perp_{r,l}\rangle$. By using the reflector, one can compose an elementary block of the QSVT circuit:

$$W = U_A^\dagger e^{i\phi_x Z_{\Pi}} U_A e^{i\phi_y Z_{\Pi}}, \quad (12)$$

where ϕ_x and ϕ_y are real scalars that can be understood as rotation angles. A sequence of copies of this operator creates a complex polynomial $P_{\text{QSVT}}(A)$ of definite parity. An odd polynomial of A with a degree not exceeding N_{pol}

can be calculated as [19]

$$P_{\text{QSVT}}^{\text{odd}}(A) = \langle 0|_{q,a} \left(e^{i\phi_0 Z_{\Pi}} U_A e^{i\phi_1 Z_{\Pi}} \prod_{k=1}^{(N_{\text{pol}}-1)/2} G_k \right) |0\rangle_{q,a}, \quad (13)$$

where

$$G_k = U_A^\dagger e^{i\phi_{2k} Z_{\Pi}} U_A e^{i\phi_{2k+1} Z_{\Pi}}. \quad (14)$$

The polynomial P_{QSVT} is defined up to a global phase and requires $N_{\text{pol}} + 1$ classically precalculated angles ϕ_i as explained in Sec. II D. In the spaces defined by Eqs. (9a)–(10b) and spanned by $|0\rangle_a |u_r\rangle$ and $|\perp_r\rangle$, as well as $|0\rangle_a |u_l\rangle$ and $|\perp_l\rangle$, the matrix polynomial becomes the scalar polynomial $p(s)$ of a real argument s . We are interested only in real polynomials, $\text{Re} p(s)$, whose circuit representation is shown in Fig. 1. (Real polynomials have only real coefficients, but map complex domains into complex images.) The ancilla register a is used to construct the block-encoding oracle U_A , and the ancilla qubit q is used to construct the controlled rotations $\exp(i\phi_k Z_{\Pi})$ (Fig. 2). The QSVT can be used to solve Eq. (1) in that it computes $|\psi_{\text{out}}\rangle = |0\rangle_{q,a} |\psi_x\rangle_{\text{input}} + |\dots\rangle$ as

$$|\psi_x\rangle_{\text{input}} = \frac{e^{i\phi_{\text{glob}}}}{\beta_{\text{sc}} \kappa_{\text{QSVT}}} A^{-1} |b\rangle_{\text{input}}, \quad (15)$$

where $|b\rangle_{\text{input}}$ is the initial state of the input register (this means $|\psi_{\text{init}}\rangle_{\text{input}} = |b\rangle_{\text{input}}$ in Fig. 1). The QSVT circuit returns $|\psi_x\rangle_{\text{input}}$ in the input register when the ancilla registers a and q are output in the zero state. The rescaling by the condition number κ_{QSVT} and the additional factor β_{sc} ensures that $\|\psi_x\| \leq 1$, and ϕ_{glob} is an arbitrary global angle. Equation (15) indicates that measurements of the state $|\psi_x\rangle$ have the success probability $\mathcal{O}(1/\kappa_{\text{QSVT}}^2)$.

Note that we distinguish the actual condition number κ of the matrix A and the condition number κ_{QSVT} that is used as a parameter in the calculation of the QSVT angles as explained below. Throughout this paper, κ is defined as the

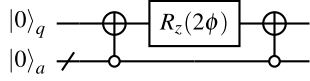


FIG. 2. The circuit of the controlled rotation $\exp(i\phi Z_{\Pi})$. Here, $R_z(2\phi) \equiv \exp(-i\phi Z)$, as in Eq. (A1c). The empty circles, called here zero-control nodes, activate the X gates if the qubit a is in the zero state. The ancilla qubits a and q are initialized in the zero state, $|0\rangle_a$ and $|0\rangle_q$, respectively.

ratio of the maximum and minimum singular values. The QSVT algorithm properly approximates A^{-1} if $\kappa_{\text{QSVT}} \gtrsim \kappa$.

For more details about the QSVT, see, for example, the recent overview in Ref. [23].

D. Computation of the QSVT angles

To compute the angles ϕ_k necessary for the construction of the QSVT circuit, one compares the polynomials $P_f(s)$ and $p(s)$. The polynomial $P_f(s)$ can be taken as a sum of Chebyshev polynomials:

$$P_f(s) = \sum_{k=0}^{N_c} c_k T_k(s). \quad (16)$$

The choice is justified in that the Chebyshev approximation is close to the minimax polynomial [24], which is the best possible polynomial approximation yet requires the application of the Remez algorithm [25], which can be computationally expensive. But the coefficients c_k can also be computed without involving the Remez algorithm, specifically, using the Fourier series

$$c_k \approx \frac{2 - \delta_{k0}}{2N_q} (-1)^k \sum_{j=0}^{2N_q-1} f[-\cos(j\pi/N_q)] e^{i(kj\pi/N_q)}, \quad (17)$$

where the number of points N_q should be not less than N_c . In our work, we use both algorithms, specifically, the numerical implementation of the Remez algorithm as presented in Ref. [26] and also our GPU-parallelized version of the Fourier-based algorithm [27].

The polynomial $p(s)$ can also be represented as a linear combination of Chebyshev polynomials with coefficients depending on ϕ_k . The general algorithm to compute ϕ_k involves comparing the polynomial coefficients in $p(s)$ and $P_f(s)$. Usually, this requires arbitrary-precision arithmetic [28,29]. In this work, however, ϕ_k are computed by minimizing the difference between $p(s)$ and $P_f(s)$ as proposed in Refs. [22,26]. This algorithm works with the standard double-precision arithmetic.

To compute the polynomial for the inverse function s^{-1} , one considers the interval $s \in [-1, -1/\kappa_{\text{QSVT}}] \cup [1/\kappa_{\text{QSVT}}, 1]$ and approximates the original function by an

auxiliary one that coincides with s^{-1} at the chosen interval and is analytic within $[-1/\kappa_{\text{QSVT}}, 1/\kappa_{\text{QSVT}}]$. For instance, one can take [30]

$$f(s) = \frac{1 - e^{-(5s\kappa_{\text{QSVT}})^2}}{s}. \quad (18)$$

Then, one can use an odd polynomial to approximate $f(s)$ with some absolute approximation error $\varepsilon_{\text{QSVT}}$:

$$|f(s) - P_f(s)| \leq \varepsilon_{\text{QSVT}}. \quad (19)$$

Our calculations show that the polynomial approximation of s^{-1} using the Remez algorithm works efficiently for small condition numbers ($\kappa_{\text{QSVT}} \lesssim 200$) and, generally, results in a smaller number of terms in $P_f(s)$ than the Fourier approach. For larger κ_{QSVT} , we use the Fourier approach since the Remez algorithm fails to deliver the coefficients of higher-order polynomials within a reasonable time. (Further optimization of the Remez algorithm, including its parallelization, might be possible but is not considered in this work.) In both cases, though, the number of terms in $P_f(x)$ grows linearly with κ_{QSVT} and logarithmically with $\varepsilon_{\text{QSVT}}^{-1}$.

III. SCALING

A. General scaling of the QSVT

Here, we consider the scaling of the QSVT algorithm and compare it with classical methods for the matrix inversion. Because it is difficult to assess how preconditioning scales with the system size in the general case [21], we consider only a conservative scaling of the problem without preconditioning. However, even in this case, a polynomial speedup of the quantum method is possible for high-dimensional problems.

According to Ref. [20], the query complexity of the QSVT algorithm scales as $\mathcal{O}[\kappa \ln(\kappa/\varepsilon_{\text{QSVT}})]$, as also validated by numerical simulations (Fig. 3). Here, we assume that the QSVT angles are computed using the parameter κ_{QSVT} close to the matrix condition number, $\kappa_{\text{QSVT}} \approx \kappa$. During each query, the QSVT circuit addresses the block-encoding oracle, which scales as $\mathcal{O}[\zeta \ln(N)]$, where N is the size of the encoded matrix A , and ζ is the matrix sparsity. According to Eq. (15), the probability of the zero-ancilla state after inverting a given matrix using the QSVT is $\mathcal{O}(1/\kappa^2)$. Therefore, subsequent amplitude estimation, which includes amplitude amplification as a subroutine, requires $\mathcal{O}(\kappa)$ repetitions of the original QSVT procedure to achieve the probability ≥ 0.5 . Thus, the algorithm complexity is

$$\mathcal{O}\left[\kappa^2 \zeta \ln(N) \ln\left(\frac{\kappa}{\varepsilon_{\text{QSVT}}}\right)\right], \quad (20)$$

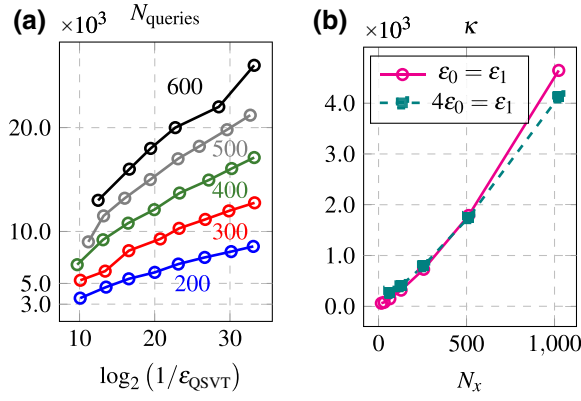


FIG. 3. (a) Query complexity, N_{queries} , versus the QSVT approximation error, $\epsilon_{\text{QSVT}} \in [10^{-3}, \dots, 10^{-12}]$, for various κ_{QSVT} indicated by the colored numbers. (b) κ versus the number of spatial points, N_x , for the systems described in Sec. IV B.

assuming that the initialization of the starting quantum state is trivial, which is true in our case as explained in Sec. V B.

B. Scaling of the algorithm for modeling classical waves

In this paper, we are focusing on modeling wave dynamics and consider measurements relevant to this problem. Usually, in such problems, the spatial distribution of the corresponding fields is discretized by a finite-difference scheme or a finite-element method (FEM) over a grid with N_x^D points (assuming the resolution is the same along all axes), where D is the number of spatial dimensions, and N_x is the number of points in the spatial grid along a single axis. This distribution is then encoded into $N_x^D N_{\text{fields}}$ complex amplitudes of the state-vector elements (Sec. V), where N_{fields} is the number of simulated variables (we assume $N_{\text{fields}} = 1$).

If one measures, for example, the wave-number spectrum in a spatial domain with N_x points by applying the quantum Fourier transform, one first needs to obtain the state projection where this spatial domain is encoded. The probability of this state equals the probability to extract N_x elements from the set with N_x^D elements (assuming that the field amplitudes are comparable at all N_x^D spatial points), so it scales as $1/N_x^{D-1}$. To increase this probability, the amplitude-amplification technique should be used, which involves $\mathcal{O}(\sqrt{N_x^{D-1}})$ repetitions of the whole QSVT circuit. Hence, the whole algorithm scales as

$$\mathcal{O}\left[\sqrt{N_x^{D-1}} \kappa^2 \zeta \ln(N_x^D) \ln\left(\frac{\kappa}{\epsilon_{\text{QSVT}}}\right)\right]. \quad (21)$$

To eliminate the factor $\sqrt{N_x^{D-1}}$ from the above equation, one can dilate the system by adding $\eta_{\text{copies}} \geq 1$ copies,

denoted as F_j , of the field amplitudes F_{j_0} at each position j_0 within the spatial domain of interest to the original state vector. Correspondingly, it is necessary to supplement the original system of equations [as the one presented in Eqs. (36) and (38)] by η_{copies} copies of the equation $F_j - F_{j_0} = 0$ for N_x positions j_0 . By adding $N_{\text{copies}} = \eta_{\text{copies}} N_x$ additional equations, one increases the desired probability up to $(1 + \eta_{\text{copies}}) N_x^{1-D}$. If $\eta_{\text{copies}} \sim \mathcal{O}(N_x^{D-1})$ (in other words, if one doubles the size of the original matrix A , $N_x^D \rightarrow 2N_x^D$), then the probability becomes $\mathcal{O}(1)$ and the scaling (21) turns into

$$\mathcal{O}\left[\kappa^2 \zeta \ln(N_x^D) \ln\left(\frac{\kappa}{\epsilon_{\text{QSVT}}}\right)\right]. \quad (22)$$

However, by adding $\eta_{\text{copies}} N_x$ equations we also increase the number of operations in the block-encoding oracle as

$$\mathcal{O}[\zeta \ln(N_x^D)] \rightarrow \mathcal{O}[\zeta \ln(2N_x^D)]. \quad (23)$$

Furthermore, the condition number of the dilated system increases as well. According to Theorem 3.1 in Ref. [31], the condition number of FEM matrices scales as $\mathcal{O}(N_{\text{full}}^{2/D})$ for $N_{\text{full}} = N_x^D$. For instance, the condition number of our one-dimensional system described in Sec. IV B scales even better, as $\mathcal{O}(N_x)$, according to the numerical results shown in Fig. 3. Thus, by doubling the matrix size, we change the condition number scaling as $\mathcal{O}(N_x^2) \rightarrow \mathcal{O}(2^{2/D} N_x^2)$. As a result, one obtains the following scaling of the QSVT for the dilated matrix:

$$\mathcal{O}\left(2^{4/D} N_x^4 \zeta \ln(2N_x^D) \left[\frac{2}{D} \ln 2 + \ln\left(\frac{N_x^2}{\epsilon_{\text{QSVT}}}\right)\right]\right). \quad (24)$$

C. Comparison with classical iterative methods

The QSVT can be compared with the best-known conjugate-gradient-based classical iterative methods for the inversion of sparse matrices. These methods [32], such as biconjugate gradient stabilized (BiCGSTAB) [33], generalized minimal residual (GMRES) [34], and transpose-free quasiminimal residual (TFQMR) [35], which work with nonsymmetric matrices, generally require preconditioning to converge. Here, we assume that they scale at least as the conjugate gradient method (which works only with symmetric matrices). As shown in Ref. [36], the number of iterations in this algorithm scales as $\mathcal{O}[\kappa \ln(1/\epsilon_{\text{QSVT}})]$, and each iteration, where the sparse matrix-vector multiplication is the main operation, scales as $\mathcal{O}(\zeta N_x^D)$. Thus, the scaling of the classical iterative method is

$$\mathcal{O}[\zeta N_x^D \kappa \ln(1/\epsilon_{\text{QSVT}})]. \quad (25)$$

Here, we take the resulting absolute error in the classically calculated signal to be ϵ_{QSVT} . Taking into account

the dependence of the condition number on the matrix size, $\kappa \sim \mathcal{O}(N_x^2)$, the classical scaling becomes

$$\mathcal{O}[\zeta N_x^{D+2} \ln(1/\varepsilon_{\text{QSVT}})]. \quad (26)$$

By comparing Eqs. (24) and (26), one can see that the QSVT becomes more efficient than the classical methods in high-dimensional problems, namely, those with $D \geq 3$. Examples of such (linear) problems include modeling of the wave propagation in plasma that is described hydrodynamically in three spatial dimensions or kinetically in six phase-space dimensions.

Let us roughly estimate how many qubits are needed for the QSVT to outperform the classical conjugate gradient method. Specifically, we focus on the number of qubits $n_x = \log_2 N_x$ that is determined by the system size. According to Eqs. (24) and (26), the QSVT requires around $C\zeta 2^{4n_x}$ gates, and the classical method requires around $\zeta 2^{n_x(D+2)}$ operations. (Logarithmic factors are omitted for simplicity.) Here, C is a large constant factor that depends on, to name a few, the implementation of the block-encoding oracle, the (machine-specific) set of elementary gates, and the mapping of the QSVT circuit to an actual quantum computer. The QSVT can provide a quantum speedup when $\zeta 2^{n_x(D+2)}/C\zeta 2^{4n_x} > 1$, or in other words, when $n_x(D-2) > \log_2(C)$.

The QSVT scaling may be improved by reducing the condition number by means of preconditioning like that described in Ref. [37]. We also stress that the QSVT algorithm currently has a bottleneck in that there are no optimized methods for calculating the rotation angles ϕ_k [used in Eq. (13)] for large condition numbers. This problem is solved for our one-dimensional system, where $\kappa \sim 500$, by using the GPU-parallelized Fourier approach described in Sec. II D. For more complex problems, one may have to consider the method for computing ϕ_k that was proposed in Ref. [30].

IV. THEORETICAL MODEL

A. Problem specification

We consider EM waves in a linear medium with a dielectric permittivity ε . For simplicity, we assume the magnetic permittivity equal to unity as is the case, for example, in classical plasmas. Then, Maxwell's equations governing the waves can be written as

$$\varepsilon \partial_t \mathbf{E} = \nabla \times \mathbf{B}, \quad (27a)$$

$$\partial_t \mathbf{B} = -\nabla \times \mathbf{E}, \quad (27b)$$

assuming units such that the speed of light equals unity. We consider the simplest model that allows investigating various measurement techniques of the wave spectrum and wave energy. Specifically, ε will be assumed a piecewise-constant function of the spatial coordinates, and we will be

interested in modeling the wave propagation across discontinuities of this function. In the absence of surface current and charge densities, the following boundary conditions are satisfied on each discontinuity of ε :

$$\mathbf{E}_{I,t} - \mathbf{E}_{II,t} = 0, \quad (28a)$$

$$\mathbf{B}_{I,t} - \mathbf{B}_{II,t} = 0, \quad (28b)$$

$$\varepsilon_I \mathbf{E}_{I,n} - \varepsilon_{II} \mathbf{E}_{II,n} = 0, \quad (28c)$$

$$\mathbf{B}_{I,n} - \mathbf{B}_{II,n} = 0, \quad (28d)$$

where \mathbf{E}_t and \mathbf{B}_t are the field components tangent to the interface, \mathbf{E}_n and \mathbf{B}_n are the field components normal to the interface between the two areas, I and II , with the permittivities ε_I and ε_{II} , respectively.

We consider a one-dimensional problem where waves propagate along the x axis. The magnetic and electric fields are polarized along the z and y axes, respectively. Hence, Eqs. (27) can be expressed in a simple form:

$$\varepsilon \partial_t E = -\partial_x B, \quad (29a)$$

$$\partial_t B = -\partial_x E, \quad (29b)$$

where we omit the subindices y and z in E_y and B_z . Also, we introduce the spatial coordinate r_x that changes from 0 to 1 and is defined as

$$r_x = x / \max(|x|). \quad (30)$$

We assume a discontinuity of ε at $r_{x,\text{int}} = 1/2$, so that we have $N_{\text{layers}} = 2$ dielectric layers of different permittivities:

$$\varepsilon = \begin{cases} \varepsilon_0, & r_x < r_{x,\text{int}}, \\ \varepsilon_1, & r_x > r_{x,\text{int}}. \end{cases} \quad (31)$$

A monochromatic source $Q = Q_0 \exp(i\omega t)$ with constant frequency ω and constant amplitude Q_0 is placed at $r_x = 1$. Assuming a steady state, the corresponding electric and magnetic fields have the form $E(t, x) = E(x) \exp(i\omega t)$ and $B(t, x) = B(x) \exp(i\omega t)$, respectively. Then, the boundary-value problem for their spatial profiles $E(x)$ and $B(x)$ is given by

$$i\omega \varepsilon_L E(x) + \partial_x B(x) = 0, \quad (32a)$$

$$i\omega B(x) + \partial_x E(x) = 0, \quad (32b)$$

with the outgoing boundary conditions at $r_x = 0$ and $r_x = 1$:

$$(i\omega - \partial_x)E|_{r_x=0} = 0, \quad (33a)$$

$$(i\omega + \partial_x)B|_{r_x=1} = Q_0, \quad (33b)$$

and

$$E(r_{x,\text{int}})|_{\text{layer } 0} = E(r_{x,\text{int}})|_{\text{layer } 1}, \quad (34a)$$

$$B(r_{x,\text{int}})|_{\text{layer } 0} = B(r_{x,\text{int}})|_{\text{layer } 1}, \quad (34b)$$

with $L = [0, 1]$. (Here, the square brackets $[i_{\text{left}}, i_{\text{right}}]$ indicate a set of all integers from i_{left} to i_{right} , including i_{left} and i_{right} . To denote the same set but excluding i_{right} , we use the parenthesis as in $[i_{\text{left}}, i_{\text{right}})$. The same notation will also be used to indicate open, $(x_{\text{left}}, x_{\text{right}})$, and closed, $[x_{\text{left}}, x_{\text{right}}]$, continuous intervals with real numbers x_{left} and x_{right} .) Note that the system is not conservative in that the wave energy is lost through radiation on the left and right boundaries and replenished by the source Q . In the left half of the spatial domain, where $r_x < r_{x,\text{int}}$, the EM field is a left-propagating wave. In the right half, the reflection at the interface between the dielectric layers results in the interference of left- and right-propagating waves and in the formation of a standing wave. Also, the wave propagating within the layer with the permittivity ε has a wave number equal to

$$k_x = \sqrt{\varepsilon}\omega. \quad (35)$$

Below, we show how to develop a QSVT algorithm for this boundary-value problem and perform quantum measurements in the corresponding circuit to infer information about the spatial spectrum and the wave energy.

B. Discretization

We discretize Eqs. (32) using the central finite difference scheme as shown in Fig. 4. Separate staggered grids, each having $N_x = 2^{n_x}$ points, are used for E and B , and each dielectric layer contains $M_x = 2^{n_x-1}$ spatial points. At the bulk spatial points, the discretized Eq. (32a) is

$$i\omega\varepsilon_L E_j + \sigma(B_j - B_{j-1}) = 0, \quad (36)$$

where $j = (M_x L + k)$ with $k = [1, M_x)$ for $L = 0$ and $k = [0, M_x)$ for $L = 1$. Also, $\sigma = (2h)^{-1}$, where $2h$ is the spatial cell size:

$$2h = x_{j+1} - x_j, \quad (37)$$

for all j . The discretized Eq. (32b) is

$$i\omega B_j + \sigma(E_{j+1} - E_j) = 0, \quad j = [0, N_x - 2]. \quad (38)$$

The EM fields satisfy the outgoing boundary conditions (33) expressed as

$$\eta_+ E_0 + \eta_- E_1 = 0, \quad (39a)$$

$$\eta_- B_{N_x-2} + \eta_+ B_{N_x-1} = Q_0, \quad (39b)$$

$$\eta_- = i\omega - h^{-1}, \quad (39c)$$

$$\eta_+ = i\omega + h^{-1}. \quad (39d)$$

Equations (36) and (38) with the boundary conditions (39) can be represented as a set of linear equations (1) where

the vector ψ stores $N_{\text{vars}} = 2$ variables, E and B :

$$\psi_{dN_x+j} = \begin{cases} E_j, & d = 0, \\ B_j, & d = 1, \end{cases} \quad (40)$$

with $j = [0, N_x)$. The right-hand-side vector b in Eq. (1) has dimension $N_{\text{vars}}N_x$ and encodes the source with the amplitude $Q_0 = 1$:

$$b_{dN_x+j} = \begin{cases} 1, & (dN_x + j) = 2N_x - 1, \\ 0, & \text{otherwise,} \end{cases} \quad (41)$$

with $j = [0, N_x)$ and $d = [0, 1]$. The $N_{\text{vars}}N_x \times N_{\text{vars}}N_x$ matrix A is represented as a sum of two matrices:

$$A = A^{\text{bulk}} + A^{\text{edge}}, \quad (42)$$

with

$$A_{kj}^{\text{bulk}} = \begin{cases} (-1)^l \sigma, & j = k + N_x - l, \quad k = [1, N_x), \\ (-1)^{l+1} \sigma, & j = k - N_x + l, \\ & k = [N_x, 2N_x), \\ i\omega, & j = k, \quad k = [N_x, 2N_x - 2], \\ i\omega\varepsilon_L, & j = k, \quad k \neq 0, \\ & k = [M_x L, M_x(L+1) - 1], \\ 0, & \text{otherwise,} \end{cases} \quad (43)$$

and

$$A_{kj}^{\text{edge}} = \begin{cases} \eta_+, & j = k, \quad k = 0 \text{ and } 2N_x - 1, \\ \eta_-, & j = k + 1 = 1, \\ & j = k - 1 = 2N_x - 2, \\ 0, & \text{otherwise,} \end{cases} \quad (44)$$

where $L = [0, 1]$, $l = [0, 1]$, and k is the row index. The matrix A^{bulk} contains information about the system evolution in the bulk spatial points. The matrix A^{edge} describes the boundary conditions.

V. ENCODING OF THE CLASSICAL SYSTEM INTO A QUANTUM CIRCUIT

Various formulations suitable for the QC of Maxwell's equations were proposed in Refs. [37–41], which considered analytical descriptions and the algorithm complexity but not actual circuits. Below, we show how to construct quantum circuits for this problem explicitly.

A. Input registers

To map the problem on a quantum circuit, we introduce two input registers. The first one, r_d , consists of one qubit and encodes the variable index: $|0\rangle_{r_d}$ for the electric field and $|1\rangle_{r_d}$ for the magnetic field. The second register, r_j ,

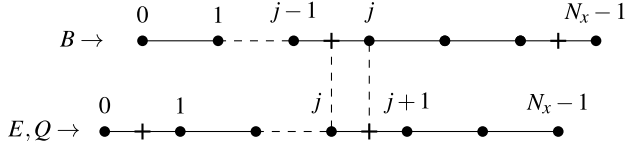


FIG. 4. The spatial domain is discretized with two staggered grids. Each grid has N_x points, and the spatial step h is defined in Eq. (37). The magnetic field is defined on the upper grid shifted by h to the right from the lower grid, on which the electric field is defined. The source Q is placed at the right boundary of the lower grid. The outgoing boundary conditions (33) on E and B are calculated in the middle of the leftmost cell of the lower grid and of the rightmost cell of the upper grid, respectively.

contains $n_x = \log_2 N_x$ qubits and encodes the coordinate index on the spatial grid. (If N_x is such that n_x is not integer, one can use $n_x = \lceil \log_2 N_x \rceil$ qubits. Then, the dimension of the vectors b and ψ and matrix A in Sec. IV B are determined by $\tilde{N}_x = 2^{n_x}$ instead of N_x .) The state amplitude corresponds to the field magnitude at a given spatial point. For instance, the amplitude of the state $|1\rangle_{r_d} |j\rangle_{r_j}$ stores the magnitude of the magnetic field at x_j , where x_j is taken on the upper spatial grid in Fig. 4. All indices are numbered starting from 0.

B. Initialization

To solve Eq. (1) with the matrix (42) and the source (41) using the QSVT, one needs to block encode the matrix A into the unitary U_A [Eq. (6)] and encode the vector b as the initial state, denoted as $|b\rangle$. At the beginning, all qubits are initialized in the zero state. Using the registers r_j and r_d , the right-hand-side vector can be encoded as

$$|b\rangle = \sum_{k=0}^{N_x-1} (\alpha_k^{(E)} |0\rangle_{r_d} |k\rangle_{r_j} + \alpha_k^{(B)} |1\rangle_{r_d} |k\rangle_{r_j}). \quad (45)$$

The coefficients $\alpha_k^{(E,B)}$ are determined from Eq. (41), whence $\alpha_k^{(E)} = 0$ for all k and $\alpha_k^{(B)} = \delta_{k, N_x-1}$. Because the bit-string encoding the number $N_x - 1$ consists only of units, the state $|b\rangle$ can be initialized by applying the X gate to each qubit in the register r_j . Also, the X gate is applied to the qubit r_d . Of note, the depth of the corresponding initialization circuit, henceforth denoted “INIT,” does not depend on N_x .

C. Block encoding of a non-Hermitian matrix

To block encode the matrix A , one should normalize it first according to Eq. (8). Here, we normalize A in the following way:

$$A \rightarrow A / (d_H^2 \|A\|_{\max}). \quad (46)$$

The origin of the factor $d_H = 2$, where d_H^2 is close to the actual sparsity of A , is explained in Sec. V E.

To block encode a non-Hermitian matrix, one usually extends it first to a Hermitian one [13,37,42]:

$$A_{\text{ext}} = \begin{pmatrix} 0 & A \\ A^\dagger & 0 \end{pmatrix}. \quad (47)$$

After that, one can use the standard state-preparation technique [4,43] to block encode A_{ext} , where the oracle U_A is represented through unitary operators O_F , O_H , O_M :

$$U_A = O_F^\dagger O_M O_H O_F. \quad (48)$$

The circuit implementing U_A operates with “input” qubit registers (in our case, registers r_j and r_d) that contain initial and final (output) data, and also ancilla registers that are initialized in the zero states and used for intermediate computations. The operator O_F reads a row index from the input registers, calculates the column indices of all nonzero elements of A_{ext} at the given row and writes the computed indices into the ancillae. The operator O_H computes the values of these nonzero elements and encodes them into the amplitudes of the ancilla-qubits’ states. The operator O_M transfers the computed column indices to the input registers so that U_A could return the indices as an output. After that, O_F^\dagger uncomputes (sets back to zero) the used ancilla registers for the state encoding the matrix nonzero elements.

In our implementation, we amend the above technique. In order to shorten the circuit for U_A , we avoid extending A to a Hermitian matrix. Instead, we split O_F into two oracles O_{bulk} and O_{edge}^F , and the adjoint O_F^\dagger is replaced with the product of O_{bulk}^\dagger and O_{edge}^B . The index “F” in O_{edge}^F stands for “forward,” and the index “B” in O_{edge}^B stands for “backward.” The pair of oracles O_{edge}^F and O_{edge}^B encodes the locations of the elements η_\pm in Eq. (44). The oracles O_{bulk} and O_{bulk}^\dagger encode the positions of the matrix elements in Eq. (43). Hence, the decomposition (48) is replaced with

$$U_A = O_{\text{bulk}}^\dagger O_{\text{edge}}^B O_M O_H O_{\text{edge}}^F O_{\text{bulk}}. \quad (49)$$

Note that $O_{\text{edge}}^B = (O_{\text{edge}}^F)^\dagger$ for a Hermitian A but not in general (Sec. V E). The decomposition (49) eliminates the need for the supplemental ancilla used for the extension (47), and one can also avoid additional gates needed for the block encoding of A^\dagger in Eq. (47). The circuit for U_A is shown in Fig. 5. To describe the action of each operator in the above product, we need to consider the ancilla qubits used in the intermediate computations.

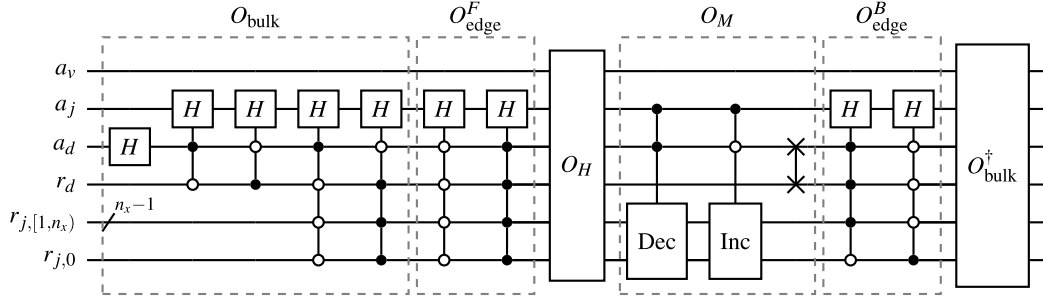


FIG. 5. The circuit implementing the oracle U_A described in Eq. (49). The circuit for the operator O_H is shown in Fig. 6. The decrementor (Dec) and incrementor (Inc) are described in Eqs. (53), and their circuits can be found in Ref. [4]. The ancillae a_d , a_j , and a_v are initialized in the zero state and described in Sec. VD.

D. Ancilla qubits

The matrix A of size $2N_x \times 2N_x$ can be separated into four blocks of size $N_x \times N_x$ each. We introduce the ancilla qubit a_d to address the first N_x columns of A when this qubit is in the zero state and to the last N_x columns when it is in the unit state. The input register r_d described in Sec. VA is used to address the first N_x matrix rows when it is in the state $|0\rangle_{r_d}$ and the last N_x rows when it is in the state $|1\rangle_{r_d}$. Hence, any block can be addressed by using just the qubits a_d and r_d .

Another ancilla, denoted a_v , is used to store the values of the matrix nonzero elements, as explained in Sec. VF.

An additional qubit, a_j , encodes the relative positions of matrix elements with respect to the diagonal within each block. The zero state of the qubit a_j indicates a matrix element on the diagonal of a given block. (The position of the block itself in the matrix A is encoded by the qubits a_d and r_d as described above.) Having a_j in the unit state encodes different information depending on the state of a_d . If a_d is in the zero state, then $|1\rangle_{a_j}$ indicates the matrix element shifted by one cell to the right from the block diagonal. If a_d is in the unit state, then $|1\rangle_{a_j}$ indicates the element shifted by one cell to the left:

$$|0\rangle_{a_j} \rightarrow i_c = i_r, \quad (50a)$$

$$|1\rangle_{a_j} \rightarrow \begin{cases} i_c = i_r + 1, & \text{if } a_d \text{ is in state } |0\rangle_{a_d}, \\ i_c = i_r - 1, & \text{if } a_d \text{ is in state } |1\rangle_{a_d}, \end{cases} \quad (50b)$$

where $i_c, i_r = [0, \dots, N_x]$ are the column and row indices, respectively, of a matrix element within a given block.

The dependence on a_d is due to the fact that in the upper and lower left blocks (corresponding to a_d 's being in the zero state), the matrix (42) has nonzero elements only on the block diagonals and in cells shifted by one cell to the right from the diagonals. In the upper and lower right blocks (corresponding to a_d 's being in the unit state), we work only with block-diagonal elements and elements shifted by one cell to the left.

E. Matrix structure

To explain the action of U_A given by Eq. (49), let us first ignore the effect of O_H and consider an auxiliary operator

$$O_S = O_{\text{bulk}}^\dagger O_{\text{edge}}^B O_M O_{\text{edge}}^F O_{\text{bulk}}. \quad (51)$$

The purpose of introducing this auxiliary operator is to explain the appearance of the factor d_H^2 in Eq. (46), which is determined by the matrices entering Eq. (51) but not O_H .

The operators O_{bulk} and O_{edge}^F (Fig. 5) encode the column indices of nonzero elements to a linear superposition of states of the ancillae a_d and a_j using a given row index from the registers r_j and r_d . For instance, for the matrix row with the index $k = 1$ (the second top matrix row encoded as $|0\rangle_{r_d} |1\rangle_{r_j}$), one has

$$O_{\text{bulk}} |0\rangle_{a_j} |0\rangle_{a_d} |0\rangle_{r_d} |1\rangle_{r_j} = (d_H^{-1/2} |0\rangle_{a_j} |0\rangle_{a_d} + d_H^{-1} |0\rangle_{a_j} |1\rangle_{a_d} + d_H^{-1} |1\rangle_{a_j} |1\rangle_{a_d}) |0\rangle_{r_d} |1\rangle_{r_j}. \quad (52)$$

Here, the first term in parenthesis encodes the position of the element $i\omega\varepsilon_0$ on the main matrix diagonal in Eq. (43) in the row with $k = 1$. The second and third terms encode the positions of the elements $(-1)^l \sigma$ in Eq. (43) at $k = 1$. Thus, the column indices are written to the states of the qubits a_d and a_j . The various orders of the factor d_H introduced in Eq. (46) appear here due to the action of Hadamard gates, because each Hadamard gate modifies the state probability by $2^{-1/2}$.

As mentioned in Sec. VC, the oracle U_A returns the state encoding matrix column indices. To transfer the column indices saved in the ancillae a_d and a_j to the input registers r_d and r_j , we use the operator O_M , where the decrementor and incrementor (“Dec” and “Inc” gates in Fig. 5) map the relative positions (encoded into the ancilla a_j) to the absolute column indices and write them to the input register r_j .

These operators act on a given state $|k\rangle$ in the following way:

$$\text{Inc } |k\rangle = |k+1\rangle, \quad (53a)$$

$$\text{Dec } |k\rangle = |k-1\rangle, \quad (53b)$$

and they are controlled by the ancillae a_j and a_d (as shown in Fig. 5) to correctly perform the mapping described in Eq. (50). Apart from that, O_M transfers the absolute column indices stored in the ancilla a_d to the input qubit r_d by swapping these qubits.

The oracle O_{edge}^B is close to $O_{\text{edge}}^{F\dagger}$, but the control nodes of the Hadamard gates in O_{edge}^B are adjusted in such a way that the operator O_S returns the correct column indices of the element η_- in Eq. (44). The oracle O_{edge}^B is found ad hoc specifically to encode the non-Hermitian matrix (42).

To describe the oracle O_H , note first that O_S does not only encode the column indices into r_d and r_j but also modifies the amplitudes of the corresponding quantum states as demonstrated in Eq. (52). Specifically,

$$\begin{aligned} & \langle k_c |_{r_j} \langle d_c |_{r_d} O_S | d_r \rangle_{r_d} | k_r \rangle_{r_j} \\ &= \begin{cases} d_H^{-1}, & d_r = d_c, k_r = k_c, l = [2, 2N_x - 3], \\ d_H^{-3/2}, & d_r = d_c, k_r = k_c, \\ & l = [0, 1] \cup [2N_x - 2, 2N_x - 1], \\ d_H^{-3/2}, & d_r \neq d_c, k_r = k_c, l = [0] \cup [2N_x - 1], \\ d_H^{-2}, & d_r = d_c, |k_c - k_r| = 1, l = [0] \cup [2N_x - 1], \\ d_H^{-2}, & d_r \neq d_c, k_c = k_r, k_r = [1, N_x - 2], \\ d_H^{-2}, & d_c = d_r + 1, k_c = k_r - 1, k_c = [0, N_x - 2], \\ d_H^{-2}, & d_c = d_r - 1, k_c = k_r + 1, k_c = [1, N_x], \end{cases} \quad (54) \end{aligned}$$

where $l = d_r N_x + k_r = [0, 2N_x)$, $d_r = [0, 1]$, $k_r = [0, N_x)$, and the ancillae a_d and a_j are assumed to be returned in the zero states. The oracle O_H must take into account the values from Eq. (54) and output the correct amplitudes A_{kj} from Eqs. (43) and (44).

F. Operator O_H

The operator O_H encodes the values A_{kj} into the state amplitudes of the qubit a_v . This is done by applying the rotation gates described in Appendix A. The corresponding rotation angles are computed by taking into account the target values from Eq. (42), denoted v_{des} , and the multiplication factors from Eq. (54), denoted c_d , that appear due to the action of the operator O_S . For instance, the value v_{des} can be encoded in the state amplitude by using the standard gate $R_x(\theta)$ acting on the zero state of the qubit a_v :

$$\begin{aligned} & R_x(\theta) (c_d |0\rangle_{a_v} |\dots\rangle + \dots) \\ &= (c_d \cos(\theta/2) |0\rangle_{a_v} - ic_d \sin(\theta/2) |1\rangle_{a_v}) |\dots\rangle + \dots, \quad (55) \end{aligned}$$

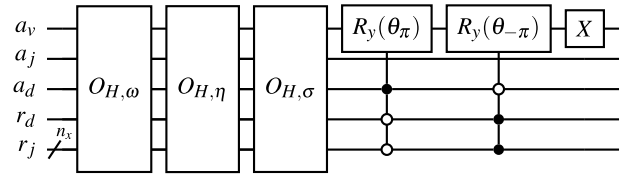


FIG. 6. The circuit implementing the operator O_H . The subcircuits are described in Fig. 7. The rotation angles $\theta_{\pm\pi}$ are computed using Eqs. (A6).

where $|\dots\rangle$ denotes states of other ancillae. The target value v_{des} can be encoded to the amplitude of either the zero state $|0\rangle_{a_v}$ or the unit state $|1\rangle_{a_v}$. Since some of the values from Eq. (42) are purely imaginary, we choose the unit state to store v_{des} , so $v_{\text{des}} = -ic_d \sin(\theta/2)$. This requires the following angle:

$$\theta = 2 \arcsin(-\iota_v |v_{\text{des}}|/c_d), \quad (56)$$

where $\iota_v = \pm 1$ is the sign of $\text{Im } v_{\text{des}}$. The above transformation works only for purely real or imaginary values. To encode a complex value, one can use the combined rotation $R_c(v)$ presented in Eq. (A4).

The circuit implementing O_H is shown in Fig. 6, and its individual blocks are detailed in Fig. 7. The rotation gates of the oracle O_H are controlled by the states of the ancillae a_d and a_j and the input registers r_d and r_j to compute the values of the matrix elements at the positions encoded in these states. The calculation of the rotation angles for the oracle O_H is summarized in Appendix A.

Assuming availability of gates that can be controlled by multiple qubits, the circuit depth of the oracle U_A scales as $\mathcal{O}(n_x)$ due to the scaling of the decrementor and incrementor operators (53). The number of ancilla qubits is independent of n_x . The main reason for this is that the ancilla a_j stores the relative positions of the matrix elements, but not the absolute column indices. (In the latter case, the number of ancillae would be proportional to n_x .) If multicontrolled gates are not available, though, they would have to be transformed into elementary gates. An n -controlled single-target gate can be transformed into $\mathcal{O}(n^2)$ elementary gates using $\mathcal{O}(n)$ ancillae [44].

VI. COMPARISON WITH CLASSICAL SIMULATIONS

A. Direct comparison without measurements

We solve the model equations (32) by computing the inverse of the corresponding matrix (42) classically (by applying the standard Gauss-Jordan elimination) and by using the QSVT, whose quantum circuit is emulated using our open-source code [27]. Two sets of parameters are considered.

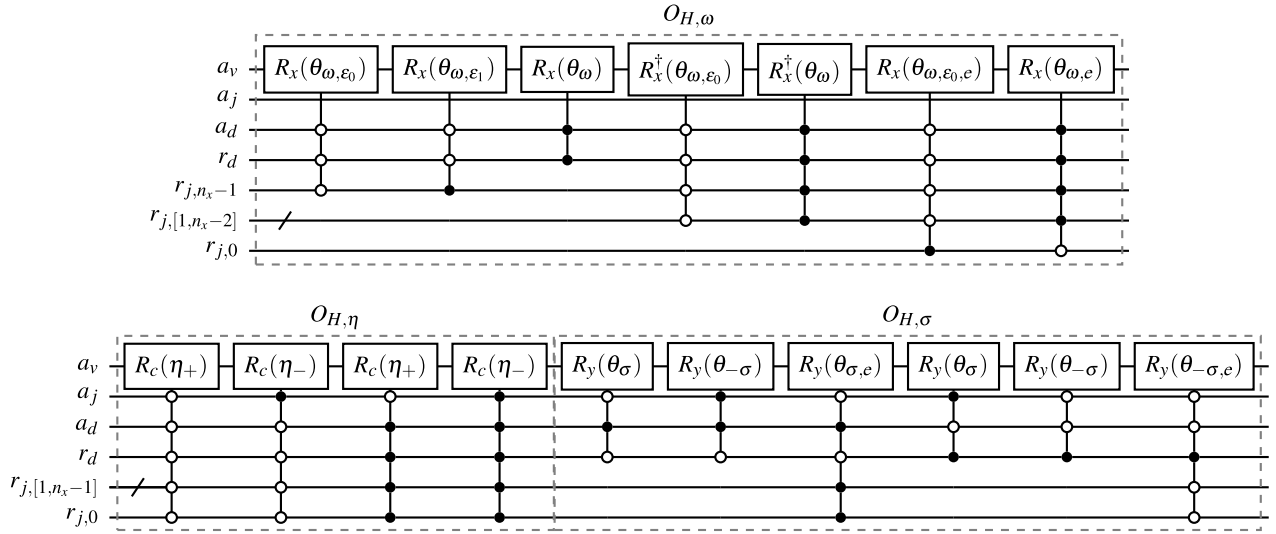


FIG. 7. The subcircuits of the circuit for O_H shown in Fig. 6. The operator R_c is described in Eq. (A4). The corresponding rotation angles are computed using Eqs. (A6).

The first set is intended to test our scheme in the simplest possible case of vacuum wave, $\epsilon_0 = \epsilon_1 = 1$, where the wave propagates to the left from a source Q placed at the right boundary. We choose the size of the simulated domain, L_x , such that we would have enough wavelengths in the simulated area to measure the wave-number spectrum. Specifically, we take $L_x k_{x,0} = 20.0$. The number of points in the spatial grid, N_x , is chosen such that classical simulations would converge. This corresponds to $n_x = 6$. Also, the corresponding matrix A had a condition number $\kappa \approx 150$, which is estimated as the ratio of the maximum and minimum singular values. (This value varies depending on the method used for calculating κ , as discussed in Ref. [16].)

The second set is intended to provide the simplest possible test of our scheme in application to inhomogeneous media, where the wave number and the wave amplitude can vary in space and reflection is possible. Like in the first case, the wave propagates to the left from a source Q placed at the right boundary. However, in this case we place a dielectric-dielectric interface at the center of the spatial domain [Eq. (31)] with $\epsilon_0 = \epsilon_1/4 = 1$. These values are chosen such that, albeit different from each other, both ϵ_0 and ϵ_1 would be order one to avoid small wavelengths (which would have required using larger resolution and more QSVT angles). When the left-propagating wave (incident wave) excited by the source Q hits this interface, the wave is partially reflected and partially transmitted to the left half of the spatial domain ($r_x < r_{x,\text{int}}$). Hence, the right half of the spatial domain ($r_x > r_{x,\text{int}}$) contains both incident and reflected waves. Their interference changes the field amplitude and the wave-number spectrum. (This will be analyzed in Secs. VIB and VIC.) Because the wave

number in the right domain is larger than in the first case, a larger number of spatial points is necessary. Hence, we use $n_x = 7$ instead of $n_x = 6$. This results in a larger condition number of the matrix A , $\kappa \approx 400$, so larger κ_{QSVT} is necessary to compute A^{-1} using the QSVT.

The comparison between the classical and QSVT simulations for these two cases is shown in Figs. 8 and 9, respectively. The QSVT angles are computed using the indicated parameter κ_{QSVT} and the approximation error ϵ_{QSVT} . (The field profiles are obtained without taking measurements into account, leveraging the fact that we emulate the circuit on a classical computer. How to extract classical information from actual quantum simulations is discussed in the next sections.) Also note that the QSVT-calculated fields in Figs. 8 and 9 are multiplied by κ_{QSVT} to account for the normalization in Eq. (15).

As seen from Figs. 8 and 9, if the QSVT parameter κ_{QSVT} is not sufficiently large, the calculation of the electric field using the QSVT does not converge. Also, as seen from the magenta and gray lines in Fig. 10, if κ_{QSVT} is not large enough, then the decrease of ϵ_{QSVT} does not improve the precision of the modeled signal (i.e., the electric field E). In other words, the parameter κ_{QSVT} , which determines the number of the QSVT angles and their values, defines the maximum achievable precision of the simulated signals. If κ_{QSVT} is sufficiently large [as mentioned in Sec. III, $\log_2 \kappa_{\text{QSVT}}$ scales as $\mathcal{O}(n_x)$], then the resulting error changes linearly with ϵ_{QSVT} . For the QSVT of classical systems with smaller n_x (and thus, with smaller condition numbers of the matrix A), smaller κ_{QSVT} suffice to avoid the saturation in the numerical precision.

By comparing Figs. 3(b) and 10, one can roughly estimate κ_{QSVT} for achieving the sought numerical precision.

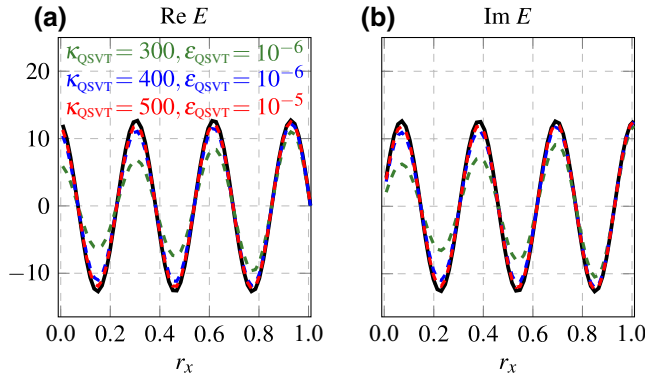


FIG. 8. Comparison of classical simulations (solid black lines) with quantum computations (colored dashed lines) done on an emulator [27,45] for $\epsilon_0 = \epsilon_1 = 1$ and $n_x = 6$: (a) $\text{Re } E(x)$, (b) $\text{Im } E(x)$. The global phase of the signals from the QC is adjusted to that of the classical signal.

In particular, to guarantee that the error in the QSVT-computed signal is around 10^{-4} (y axis in Fig. 10), $\kappa_{\text{QSVT}} = 200$ is enough for $n_x = 4$, where $\kappa = 60$. For $n_x = 5$ ($\kappa = 80$), one needs $\kappa_{\text{QSVT}} = 300$. For $n_x = 6$ ($\kappa = 150$), one needs at least $\kappa_{\text{QSVT}} = 500$. Thus, $\kappa_{\text{QSVT}}/\kappa \gtrsim 3$ is needed to guarantee the error 10^{-4} . That said, for modeling a system with a different A , one might need to perform a convergence test similar to that in Fig. 10 to estimate the minimum κ_{QSVT} for given desired precision.

B. Estimation of the wave numbers

One can estimate the dominant wave number(s) of the electric field using the quantum Fourier transform (QFT). A possible circuit is shown in Fig. 11. If one needs to measure the spectrum only in the left (right) half of the spatial domain, then the X gate should be controlled also

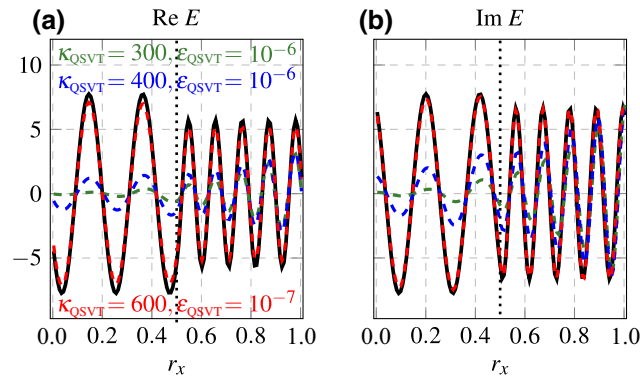


FIG. 9. Comparison of classical simulations (solid black lines) with quantum computations (colored dashed lines): (a) $\text{Re } E(x)$, (b) $\text{Im } E(x)$. The parameters are $4\epsilon_0 = \epsilon_1 = 4$ and $n_x = 7$. The black dotted vertical lines indicate the boundary where the dielectric permittivity changes abruptly.

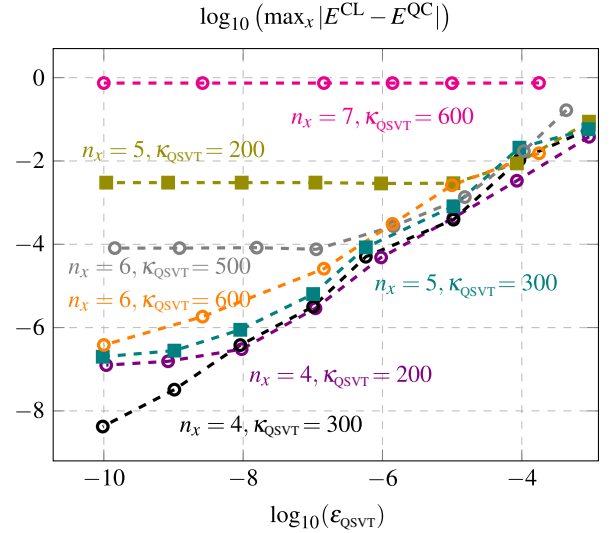


FIG. 10. The dependence of the maximum absolute difference between the electric fields calculated classically and by the QSVT on the absolute error ϵ_{QSVT} for different values of κ_{QSVT} and n_x for $\epsilon_0 = \epsilon_1 = 1$.

by the zero (unit) state of the uppermost qubit in the register r_j . The zero-control node on the qubit r_d entangles the unit state $|1\rangle_m$ in the qubit m with the state returned by the QSVT subcircuit encoding the spatial distribution of the electric field. As seen from Eq. (15), the amplitude of this state scales as $\mathcal{O}(1/\kappa)$. Thus, the state should be amplified by using the amplitude amplification (AA) procedure (“AAb”) [47] for an unknown amplitude that requires $\mathcal{O}(\kappa)$ repetitions of the circuit U_{prep} presented in Fig. 11. After the “AAb,” the probability to measure $|1\rangle_m$ becomes not less than $1/2$.

If the unit state $|1\rangle_m$ is measured, then the QFT, which requires $\mathcal{O}(n_x^2)$ quantum gates, is performed in the register

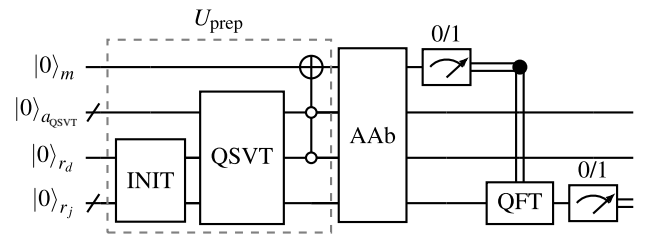


FIG. 11. The circuit that measures the wave number of the stationary electric field E in the whole spatial domain. The register a_{QSVT} includes all ancilla qubits necessary for the QSVT circuit (i.e., the registers a_d , a_j , a_v , and q). The QSVT circuit is presented in Fig. 1. The QFT is a well-known circuit in QC and is described in detail in Ref. [46]. The amplitude amplification procedure (denoted here as “AAb”) for an unknown amplitude is described in Ref. [47]. Here, the QFT is performed only if the qubit m is measured in the unit state, otherwise the whole circuit should be restarted.

r_j . Specifically, the spatial distribution of the electric field over the grid

$$x = j \Delta x, \quad j = [0, N_x), \quad (57)$$

is transformed into its spectrum on the wave-number grid

$$k_x = -k_{\max} + \Delta k j, \quad j = [0, N_x), \quad (58)$$

where $k_{\max} = \pi/\Delta x$, $\Delta x = 2h$, $\Delta k = 2k_{\max}/N_x$, and N_x is an even integer (Sec. IV B). More precisely, after the QFT, the bit strings in the register r_j encode the wave-number grid, and the state amplitudes encode the corresponding Fourier magnitudes. The measurement of the qubits in the register r_j outputs a bit string encoding a single wave number k_x of a Fourier component with some amplitude F_{k_x} . The probability to measure a certain k_x equals $|F_{k_x}|^2$.

Since the circuit shown in Fig. 11 is computationally expensive to emulate classically, we compute it in parts by modeling the INIT + QSVT circuit first and then transferring the computed QSVT state directly to the QFT as an input. The comparison between the classical FFT and QFT is shown in Fig. 12, where both FFT and QFT are defined over the same wave-number grid (58). Specifically, shown in Fig. 12 is the distribution of the probability with which a measurement returns a given k_x . According to the figure, each measurement most likely returns the wave numbers $k_{x,0}$ or $\sqrt{\varepsilon_1}k_{x,0}$, which is in agreement with Eq. (35).

This QFT-based procedure is particularly useful when the wave spectrum consists mainly of just a few dominant modes, which can be identified with $\mathcal{O}(1)$ measurements. A relevant application could be to the modeling of radiofrequency modes in fusion plasmas [48], where the local spectrum often consists of a mode launched by an antenna and, possibly, few other modes generated by reflection and (or) mode conversion [49]. The corresponding wave vectors vary in space, and the above procedure can be used to identify these wave vectors at a given location of interest.

C. Amplitude estimation of the field energy

To measure the field energy summed over a chosen spatial domain, we can use the so-called amplitude-estimation (AE) procedure. For example, it can be implemented using the standard algorithm described in Ref. [47]. The corresponding circuit is shown in Fig. 13, where the register r_y has n_y qubits. There, the subcircuit U_{prep} entangles the unit state $|1\rangle_m$ with the superposition of states encoding the spatial distribution of the electric field in the right domain ($r_x > r_{x,\text{int}}$):

$$\psi_E = |1\rangle_m \left(|0\rangle_{r_d} \sum_{j=N_x/2}^{N_x-1} E_j |j\rangle_{r_j} \right) + |0\rangle_m (\dots). \quad (59)$$

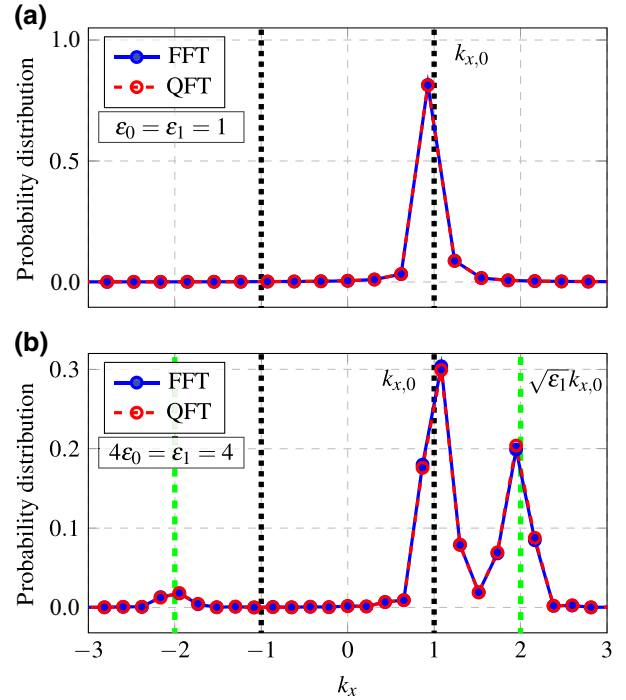


FIG. 12. A comparison of the results obtained using classical FFT (solid blue lines and markers) and the QFT (dashed red lines and markers): (a) $\varepsilon_0 = \varepsilon_1 = 1$, $n_x = 6$, $\kappa_{\text{QSVT}} = 500$, $\varepsilon_{\text{QSVT}} = 10^{-5}$; (b) $4\varepsilon_0 = \varepsilon_1 = 4$, $n_x = 7$, $\kappa_{\text{QSVT}} = 600$, $\varepsilon_{\text{QSVT}} = 10^{-7}$. The vertical black lines correspond to $k_x = \pm k_{x,0}$. The vertical green lines correspond to $k_x = \pm \sqrt{\varepsilon_1} k_{x,0}$. Here, the wave-number grid is normalized to $k_{x,0} = \omega$.

[Here, we omit the register r_y , which remains in the zero state. We also omit the multiplication factor from Eq. (15) and the QSVT ancillae.] The electric field energy can be measured as the probability amplitude of the state $|1\rangle_m$:

$$p_{m,1} = \sum_{j=N_x/2}^{N_x-1} |E_j|^2. \quad (60)$$

Instead of emulating the circuit from Fig. 13 directly, which is computationally expensive, we emulate a simplified circuit shown in Fig. 14. There, the operator U_{prep} is reduced to the one-qubit rotation $R_y(\theta_E)$, so

$$U_{\text{sim}} |0\rangle_m = \cos(\theta_E) |0\rangle_m + \sin(\theta_E) |1\rangle_m, \quad (61)$$

where $\sin^2(\theta_E) = p_{m,1}$. [This defines θ_E up to a modulo π , which is not significant since we are only interested in $\sin^2(\theta_E)$.] More precisely, we emulate the actual circuit U_{prep} to compute the state ψ_E , from which we calculate the probability $p_{m,1}$ numerically. As a result, we can find the angle θ_E . After that, we model the circuit shown in Fig. 14 using U_{sim} with the precomputed θ_E . To demonstrate the

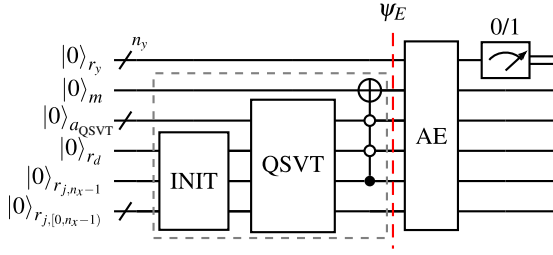


FIG. 13. The circuit for measuring the electric field energy in the right spatial domain by using the AE. The state ψ_E is described in Eq. (59) and prepared by the subcircuit U_{prep} indicated here by the dashed box.

operation of the AE, we also report emulation of the non-simplified AE circuit (as in Fig. 13) for a Gaussian field profile in Appendix B 2.

The bit string measured after the AE encodes an integer i_y from which one can estimate the desired probability amplitude [47]:

$$\tilde{p}_{m,1} = 1 - \sin^2\left(\frac{\pi i_y}{N_{\text{AA}}}\right), \quad (62)$$

where $N_{\text{AA}} = 2^{n_y}$, and $\tilde{p}_{m,1}$ is the estimated probability of the state $|1\rangle_m$. With a probability more than 0.81, the measurement outcomes $\tilde{p}_{m,1}$ with the following absolute error [47]:

$$\delta \equiv |p_{m,1} - \tilde{p}_{m,1}| \leq 2\pi \frac{\sqrt{p_{m,1}(1-p_{m,1})}}{N_{\text{AA}}} + \frac{\pi^2}{N_{\text{AA}}^2}. \quad (63)$$

Since $p_{m,1}$ is unknown in advance, in practice one can estimate δ by replacing $p_{m,1}$ with $\tilde{p}_{m,1}$ (obtained from measurements) in the right-hand side of Eq. (63). Then, the field energy stored in a given domain spanning $N_{x,\text{area}}$ points can be estimated as

$$\tilde{\mathcal{E}} = \frac{(\beta_{\text{sc}}\kappa)^2}{N_{x,\text{area}}} (\tilde{p}_{m,1} \pm \delta). \quad (64)$$

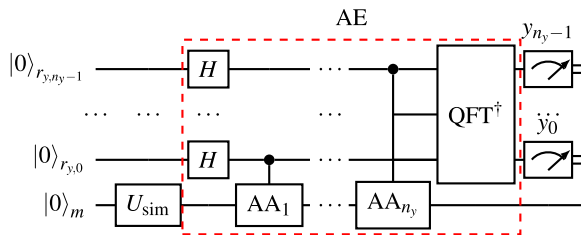


FIG. 14. The circuit used for estimating $\tilde{p}_{m,1}$. The subcircuit U_{sim} is a reduced version of the circuit U_{prep} shown in the dashed box in Fig. 13. The circuit within the red dashed box corresponds to the AE block in Fig. 13. The notation AA_m denotes 2^{m-1} applications of the AA operator (Appendix B 2).

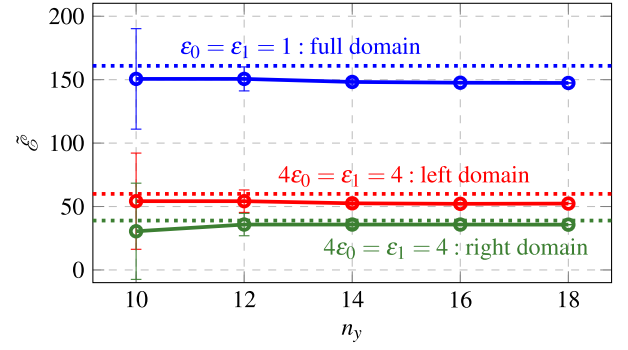


FIG. 15. The change of the estimated energy $\tilde{\mathcal{E}}$ with the number of qubits in the register r_y . The AE of the energy integrated over the full spatial domain in the case with $\epsilon_0 = \epsilon_1 = 1$ is indicated by the blue markers. The AE of the energy summed over the left domain $r_x < r_{x,\text{int}}$ or the right domain $r_x > r_{x,\text{int}}$ in the case with $4\epsilon_0 = \epsilon_1 = 4$ is indicated by the red and green markers, respectively. The horizontal dotted lines indicate the corresponding energies computed in classical simulations.

The AE circuit requires $\mathcal{O}(N_{\text{AA}})$ repetitions of the AA operator, which is described in Appendix B 2 and includes two calls to the QSVT. Because δ scales as $\mathcal{O}(1/N_{\text{AA}})$, to measure the energy with an absolute error not larger than δ , one needs $\mathcal{O}(1/\delta)$ queries to the QSVT circuit. Since the amplitude of the QSVT resulting state, where the system fields are encoded, is $\mathcal{O}(1/\kappa)$, δ should also be at least as small as $\mathcal{O}(1/\kappa)$. Thus, the AE requires $\mathcal{O}(\kappa)$ queries to the QSVT circuit. Advanced AE methods [50] can be used to reduce the number of ancillae in the AE and possibly reduce the constant coefficient hidden in the aforementioned scaling, but the scaling itself remains the same.

The results of our emulations of the above AE procedure are summarized in Fig. 15. By increasing the number of qubits in the register r_y , one can reduce the measurement error δ so that the QSVT approximation error dominates over δ . In turn, the QSVT error itself can be reduced by increasing κ_{QSVT} and (or) decreasing ϵ_{QSVT} as described in Sec. VI A.

We can also roughly estimate the number of qubits necessary for the AE of $\tilde{\mathcal{E}}$ in a D -dimensional boundary-value problem with N_v variables. To address each variable, one will need $n_d = \lceil \log_2 N_v \rceil$ qubits in the register r_d (Fig. 5). To describe the spatial distribution of these variables, Dn_x qubits are required in the register r_j . For the block encoding, one will need n_d additional qubits in the ancilla register a_d . Apart from that, similar to Eq. (50), each qubit in a_j will encode matrix column indices in a matrix sub-block associated with a particular spatial axis, thus, the register a_j will have at least D qubits. If one increases the number of points in the stencil of the difference scheme for spatial derivatives, then the register a_j will need more qubits,

i.e., $a_j = Dn_c$, where $n_c = \lceil \log_2 N_c \rceil$ and N_c is the number of spatial points in the stencil [in our case, $N_c = 2$ as one can see from Eq. (36) or Eq. (38)]. Also, we need one supplemental qubit (the ancilla q in Fig. 1) to construct the QSVT circuit. To estimate $\tilde{\mathcal{E}}$ with an absolute error $\delta = \mathcal{O}(\tilde{\mathcal{E}})$, one needs $n_y = \log_2(\tilde{\mathcal{E}}^{-1})$ qubits in the register r_y [one can see it from Eq. (63)], and at least one qubit in the register m in Fig. 13. To sum up, the resulting number of qubits will be approximately equal $D \log_2 N_x + 2 \lceil \log_2 N_v \rceil + D \lceil \log_2 N_c \rceil + 2 + \log_2(\tilde{\mathcal{E}}^{-1})$.

D. Measurement of the absorbed wave power

Another useful parameter to measure in simulations of stationary waves is the absorbed power. In a given region (x_B, x_E) , this power can be calculated as [48]

$$\mathcal{P} = \frac{1}{2} \int_{x_B}^{x_E} dx E^*(x) \int_{-\infty}^{+\infty} dx' \sigma(x, x') E(x'), \quad (65)$$

where σ is the conductivity at a given frequency, and the symbol $*$ denotes the complex conjugation. The integration over x' can be replaced by integration over $\zeta = x' - x$:

$$\mathcal{P} = \frac{1}{2} \int_{x_B}^{x_E} dx E^*(x) \int_{-\zeta_w}^{+\zeta_w} d\zeta \sigma(x, x + \zeta) E(x + \zeta), \quad (66)$$

where the domain in the second integral can be finite and arbitrary as long as it is much larger than the localization scale of σ with respect to ζ at a given x . Let us also adopt, for simplicity, that the interval (x_B, x_E) is small enough so the dependence of σ on x on this interval can be neglected. In other words, let us assume, say, $\sigma(x, x + \zeta) \approx \bar{\sigma}(x_C, \zeta)$, where $x_C = (x_B + x_E)/2$ is the center of the interval. [Further, for simplicity, we omit x_C and the bar in $\bar{\sigma}(x_C, \zeta)$.] Then, after discretization, Eq. (66) becomes

$$\mathcal{P} = \frac{D}{2N_w N_{EB}}, \quad (67a)$$

$$D = \sum_{k=k_B}^{k_E} E_k^* \sum_{j=-N_{h,w}}^{N_{h,w}} \sigma_j E_{k+j}, \quad (67b)$$

where the indices k_B and k_E correspond to the spatial points x_B, x_E , respectively. The spatial interval has $N_{EB} = k_E - k_B + 1$ points, and the electric current $\sigma_j E_{k+j}$ at the point x_k is induced by the electric field within the window of $N_w = 2N_{h,w} + 1$ points centered at x_k . To encode N_{EB} and N_w spatial points, one needs $n_{EB} = \lceil \log_2 N_{EB} \rceil$ and $n_w = \lceil \log_2 N_w \rceil$ qubits, respectively. Positive \mathcal{P} corresponds to the wave power absorbed by the environment, e.g., plasma.

In practice, σ_j depends on the given medium and is supposed to be calculated analytically or numerically in

kinetic simulations [51]. Here, we assume that the conductivity is a Gaussian function, $\sigma_j = G_j$, and rewrite Eq. (67b) as follows:

$$D = \sum_{k=0}^{N_x-1} \sum_{p=0}^{N_x-1} M_{k,p} E_k^* E_p, \quad (68)$$

with a matrix

$$M_{k,p} = \Theta_{k-k_B} \Theta_{k_E-k} G_{p-k} \Theta_{p-(k-N_{h,w})} \Theta_{(k+N_{h,w})-p}, \quad (69)$$

and Heaviside functions Θ . The sum (68) has the form of the inner product $\langle E | M | E \rangle$ and, therefore, its circuit representation can be computed by applying the Hadamard test [52,53], provided that the matrix M is encoded into a unitary one. Yet, the block encoding of M into a unitary can be difficult. Therefore, we propose an alternative way based on the SWAP test [54] and quantum arithmetic operators.

The idea is to keep the simple vector form G_j of the conductivity [instead of its matrix form G_{p-k} as in Eq. (68)]. Hence, we rewrite D in Eq. (67b) as

$$D = \sum_{k=0}^{N_{EB}-1} E_{k_B+k}^* \sum_{j=0}^{N_w-1} G_j E_{k_B+k+j-N_{h,w}}. \quad (70)$$

Here, the Gaussian G_j depends on a single index and can be calculated by the QSVT as explained in Appendix B 1. However, now the electric fields are summed over different spatial intervals and should be encoded into states on two different registers, I and II . These intervals can be set by applying various arithmetic operators described in Appendix A 3. The coupling of the electric fields in Eq. (70) through the index k can be implemented by using a quantum subtractor that performs the transformation $|k\rangle |p\rangle \rightarrow |k\rangle |p-k\rangle$.

The SWAP test computes the product of the form $|\langle \psi | \lambda \rangle|^2$ of two quantum states $|\psi\rangle$ and $|\lambda\rangle$ calculated in two separate qubit registers. In other words, one finds the square of the sum $\sum_j \psi_j^* \lambda_j$. To find the double sum as Eq. (70), we introduce supplemental registers, r_{EB} and r_w , and perform one SWAP test between the registers II and r_{EB} , and another SWAP test between I and r_w . The circuit for the computation of the double sum (70) is shown in Fig. 16, where the electric fields are computed using the QSVT subcircuits denoted ‘‘MI.’’ (‘‘MI’’ is the same QSVT circuit as the one used in Figs. 11 and 13.) Further, we consider the circuit shown in Fig. 16 step by step.

First of all, we compute the spatial distribution of the electric fields and initialize the registers r_w and r_{EB} :

$$|\xi_1\rangle = \sum_{k=0}^{N_x-1} E_k |k\rangle_{II} |\phi_{(I)}^{EB}\rangle_{r_{EB}} \sum_{p=0}^{N_x-1} E_p |p\rangle_I |\phi_{(I)}^w\rangle_{r_w}, \quad (71)$$

where all other qubits are in the zero state, and the state $|\xi_1\rangle$ is indicated in Fig. 16. The registers r_{EB} and r_w encode

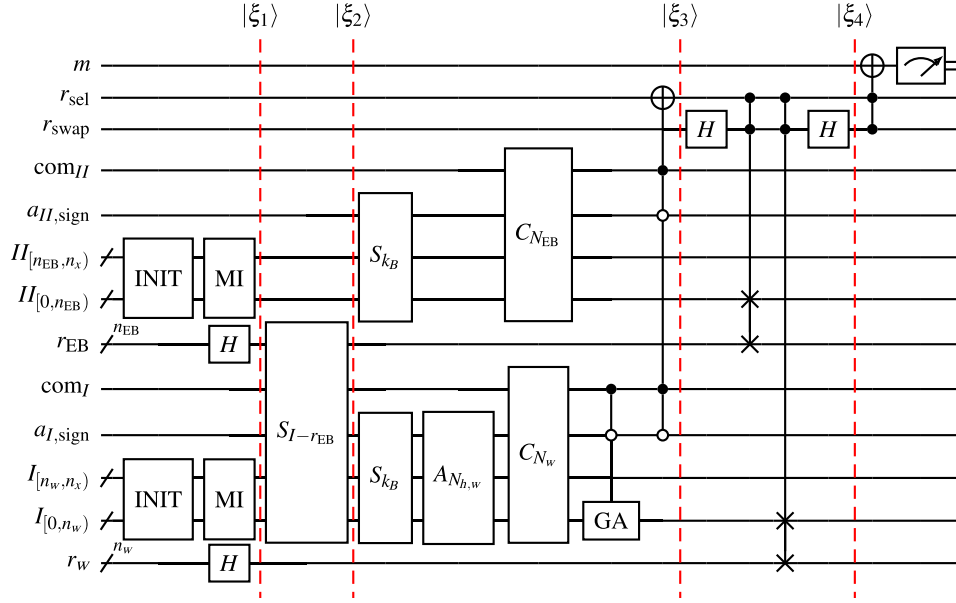


FIG. 16. A possible circuit that can be used to compute $p_{1,r_{\text{swap}}}$ [Eq. (78)], which is the probability to have both qubits r_{swap} and r_{sel} in the unit state. All qubits are initialized in the zero state. The subcircuits “MI” and “GA” are the QSVTs to compute the electromagnetic field E and the Gaussian, respectively. For clarity, we do not show here all the ancilla qubits necessary for the QSVT procedures and the register d assuming that the “MI” outputs a state encoding only the electric field. The operators S_{I-r_l} and S_{k_B} are two types of subtractors described in Appendix A 3. The adder A_i and comparator C_i (for some integer i) are also presented in Appendix A 3. The qubit com_I is not used by the subtractor S_{I-r_l} . To compute $p_{0,r_{\text{swap}}}$, the rightmost Toffoli gate must be controlled by the zero state of the qubit r_{swap} .

the following superpositions:

$$|\phi_{[l]}^{\text{EB}}\rangle = \eta_{\text{EB}} \sum_{l=0}^{N_{\text{EB}}-1} |l\rangle, \quad |\phi_{[i]}^w\rangle = \eta_w \sum_{i=0}^{N_w-1} |i\rangle, \quad (72)$$

with the constants

$$\eta_{\text{EB}} = 2^{-n_{\text{EB}}/2}, \quad \eta_w = 2^{-n_w/2}. \quad (73)$$

In Eqs. (72), the subindices indicating the qubit registers are skipped, since the states $|\phi_{[l]}^{\text{EB}}\rangle$ and $|\phi_{[i]}^w\rangle$ will also appear in other registers.

After that, the subtractor $S_{I-r_{\text{EB}}}$ couples the indices in the registers I and r_{EB} :

$$|\xi_2\rangle = \eta_{\text{EB}} \sum_{k=0}^{N_x-1} E_k |k\rangle_{II} \sum_{l=0}^{N_{\text{EB}}-1} |l\rangle_{r_{\text{EB}}} \sum_{p=0}^{N_x-1} E_p |p-l\rangle_I |\phi_{[i]}^w\rangle_{r_w}. \quad (74)$$

The expression in the rightmost sum can be recasted as $E_{l+j} |j\rangle_I$ by setting $j = p - l$, where $j = [-l, N_x - l]$. The subtractor $S_{I-r_{\text{EB}}}$ uses the ancilla $a_{I,\text{sign}}$ as a flag (or as a sign bit), which is set into the unit state for negative values of the index j . For simplicity, this ancilla is skipped in Eq. (74). Later, the state of this ancilla are taken into account to deal only with positive values of j .

The next step is to encode the electric field amplitudes at the spatial points with indices $[k_B, k_E]$ into the first n_{EB} least-significant qubits in the register II . To do that, we apply the subtractor S_{k_B} to the register II . This operator subtracts the (unsigned) integer k_B from the integers encoded within the register II and entangles all indices not less than k_B with the zero state of the qubit $a_{II,\text{sign}}$. After that, the comparator $C_{N_{\text{EB}}}$ is applied to set the correct upper limit in the sum \sum_k by entangling all indices k less than N_{EB} with the unit state $|1\rangle_{\text{com}_{II}}$.

Similar arithmetic operators are applied to the register I to entangle the intervals $[x_{k_B+l-N_{h,w}}, x_{k_B+l+N_{h,w}}]$ for $l = [0, N_{\text{EB}}]$ with the state $|1\rangle_{\text{com}_I} |0\rangle_{a_{I,\text{sign}}}$.

After that, the QSVT circuit is applied to the first n_w least-significant qubits of the register I to multiply the electric field by the Gaussian as described in Appendix B 3. To center correctly the Gaussian within the window $[x_{k_B+l-N_{h,w}}, x_{k_B+l+N_{h,w}}]$, one can use Eqs. (B3). The resulting data are entangled with the unit state $|1\rangle_{r_{\text{sel}}}$:

$$\langle 1|_{r_{\text{sel}}} |\xi_3\rangle = |\phi^E\rangle_{II} |\phi_{[l]}^{\text{EB}}\rangle_{r_{\text{EB}}} |\phi_l^G\rangle_I |\phi_{[i]}^w\rangle_{r_w}, \quad (75)$$

where the following states are used:

$$|\phi^E\rangle = \sum_{k=0}^{N_{\text{EB}}-1} E_{k_B+k} |k\rangle, \quad (76a)$$

$$|\phi_l^G\rangle = \sum_{j=0}^{N_w-1} G_j E_{k_B+l+j-N_{h,w}} |j\rangle, \quad (76b)$$

and we are not interested in the state $|0\rangle_{r_{\text{sel}}}$. Note that in Eq. (75), the double sum $\sum_l |l\rangle_{r_{\text{EB}}} \sum_j G_j E_{k_B+l+j-N_{h,w}} |j\rangle_I$ is written as $|\phi_{\{l\}}^{\text{EB}}\rangle_{r_{\text{EB}}} |\phi_l^G\rangle_I$, where the subindex l in $|\phi_l^G\rangle$ indicates the coupling to the state $|\phi_{\{l\}}^{\text{EB}}\rangle$.

To compute the absolute value of D from Eq. (70), we perform the SWAP test:

$$\begin{aligned} \langle 1|_{r_{\text{swap}}} \langle 1|_{r_{\text{sel}}} |\xi_4\rangle &= \frac{1}{2} (\langle \phi^E \rangle_{II} \langle \phi_{\{l\}}^{\text{EB}} \rangle_{r_{\text{EB}}} \langle \phi_l^G \rangle_I \langle \phi_{\{i_1\}}^w \rangle_{r_w} \\ &- \langle \phi_{\{p\}}^{\text{EB}} \rangle_{II} \langle \phi^E \rangle_{r_{\text{EB}}} \langle \phi_{\{i_2\}}^w \rangle_I \langle \phi_p^G \rangle_{r_w}). \end{aligned} \quad (77)$$

By applying the corresponding Toffoli gate, one can entangle $\langle 1|_{r_{\text{swap}}} \langle 1|_{r_{\text{sel}}} |\xi_4\rangle$ with the unit state $|1\rangle_m$ and measure its probability $p_{1,r_{\text{swap}}}$ by using the AE. The probability of the state (77) is

$$p_{1,r_{\text{swap}}} = \frac{\eta_{\text{EB}}^2 \eta_w^2}{2} (|c_0|^2 - S), \quad (78)$$

with an unknown $|c_0|^2$. The positive real value S is computed as a product of the sum:

$$\begin{aligned} &\langle \phi_{\{p\}}^{\text{EB}} | \phi^E \rangle_{II} \langle \phi_p^G | \phi_{\{i_1\}}^w \rangle_{r_w} \\ &= \sum_{p=0}^{N_{\text{EB}}-1} E_{k_B+p} \sum_{i_1=0}^{N_w-1} G_{i_1}^* E_{k_B+p+i_1-N_{h,w}}^*, \end{aligned} \quad (79)$$

with the sum

$$\begin{aligned} &\langle \phi^E | \phi_{\{l\}}^{\text{EB}} \rangle_{r_{\text{EB}}} \langle \phi_{\{i_2\}}^w | \phi_l^G \rangle_I \\ &= \sum_{l=0}^{N_{\text{EB}}-1} E_{k_B+l}^* \sum_{i_2=0}^{N_w-1} G_{i_2} E_{k_B+l+i_2-N_{h,w}}. \end{aligned} \quad (80)$$

By comparing Eq. (70) with Eqs. (79) and (80), one can see that $S \equiv |D|^2$.

The constant $|c_0|^2$ can be eliminated by measuring also $p_{0,r_{\text{swap}}}$, which is the probability of the state $\langle 0|_{r_{\text{swap}}} \langle 1|_{r_{\text{sel}}} |\xi_4\rangle$. Because this state is the same as Eq. (77) but with the “+” sign in the brackets, its probability is

$$p_{0,r_{\text{swap}}} = \frac{\eta_{\text{EB}}^2 \eta_w^2}{2} (|c_0|^2 + |D|^2). \quad (81)$$

Thus, the absolute value of the double sum (70) can be calculated as

$$|D| = \frac{1}{\eta_{\text{EB}} \eta_w} \sqrt{p_{0,r_{\text{swap}}} - p_{1,r_{\text{swap}}}}. \quad (82)$$

As mentioned before, the amplitude of the QSVT output state (returned by “MI”) is $\mathcal{O}(1/\kappa)$. To compute the

sum (70), one launches the “MI” twice in parallel to compute the product E^*E , which is $\mathcal{O}(1/\kappa^2)$. Thus, to estimate $p_{0,r_{\text{swap}}}$ or $p_{1,r_{\text{swap}}}$, one will need $\mathcal{O}(\kappa^2)$ queries to the QSVT circuit. However, if N_{EB} is comparable with the system size, then the number of the queries can be reduced at least to $\mathcal{O}(\kappa)$ for two- and three-dimensional spatial systems.

VII. CONCLUSIONS

In this paper, we propose a quantum algorithm for simulating dissipative waves in inhomogeneous linear media as a boundary-value problem. Our algorithm is based on the QSVT, which is a state-of-the-art technique that was previously proposed for other problems but is applied here to a boundary-value wave problem for the first time. Specifically, we model an EM wave that is excited by a prescribed source and propagates in a dielectric medium with a piecewise-continuous dielectric function. We show how to encode the corresponding non-Hermitian matrix in a quantum circuit, calculate the field distribution using this circuit, and perform measurements of the spatial spectrum, wave energy, and power dissipation for this and similar wave problems. We emulate quantum simulations of this circuit on a classical computer and show that the numerical results are in agreement with theory and usual classical simulations. Most of the quantum circuits presented in this paper are constructed and computed using our computational framework [27].

We also show that the overall quantum simulations of dissipative waves based on the QSVT scale favorably compared to classical simulations in multidimensional systems. We expect the gain to be particularly efficient in kinetic plasma problems, where the wave modeling is done in phase space with six or even more dimensions. Still, there are several potential problems for practical applications of the QSVT, which should be pointed out. First of all, the encoding of the considered wave classical system requires at least $4 + n_x$ qubits and the resulting QSVT circuit involves hundreds of calls to the block-encoding oracle, even without taking into account the measurements. Quantum hardware with such specifications is unlikely to appear in the foreseeable future. Another issue is that typical classical wave systems are characterized by matrices with large condition numbers. Since the QSVT used for the inversion of such matrices returns a state whose amplitude scales as $\mathcal{O}(1/\kappa)$, the measurement of the state requires $\mathcal{O}(\kappa)$ queries to the QSVT circuit. This can significantly reduce the quantum speedup. Apart from that, to invert a matrix with a large condition number, one needs to precompute classically a significant number of QSVT angles. This is difficult to do using the codes that are currently available for calculating such angles. In our case, the GPU parallelization of the code responsible for the polynomial approximation of the inverse function allowed us to compute the QSVT angles only for $\kappa_{\text{QSVT}} \lesssim 1000$

(Sec. II D). This means that quantum modeling of classical wave systems is limited and, in practice, will likely require efficient preconditioning of the dispersion matrices. (A similar problem is known for classical modeling of large wave systems [55].) For instance, due to the sparsity of the matrices associated with the computation of EM waves (such as those in cold plasmas [4]), a quantum version of the sparse approximate inverse preconditioner proposed in Ref. [37] may be useful.

ACKNOWLEDGMENTS

The research described in this paper is conducted under the Laboratory Directed Research and Development (LDRD) Program at Princeton Plasma Physics Laboratory, a national laboratory operated by Princeton University for the U.S. Department of Energy under Prime Contract No. DE-AC02-09CH11466. The author(s) are pleased to acknowledge that the work reported on in this paper is substantially performed using the Princeton Research Computing resources at Princeton University, which is a consortium of groups led by the Princeton Institute for Computational Science and Engineering (PICSciE) and Office of Information Technology's Research Computing. The authors also thank Yulong Dong for valuable discussions.

APPENDIX A: BASIC AND SUPPLEMENTAL GATES

1. Rotation gates

The following rotation gates are used throughout the paper:

$$R_x(\theta) = \begin{pmatrix} \cos \frac{\theta}{2} & -i \sin \frac{\theta}{2} \\ -i \sin \frac{\theta}{2} & \cos \frac{\theta}{2} \end{pmatrix}, \quad (\text{A1a})$$

$$R_y(\theta) = \begin{pmatrix} \cos \frac{\theta}{2} & -\sin \frac{\theta}{2} \\ \sin \frac{\theta}{2} & \cos \frac{\theta}{2} \end{pmatrix}, \quad (\text{A1b})$$

$$R_z(\theta) = \begin{pmatrix} e^{-i\theta/2} & 0 \\ 0 & e^{i\theta/2} \end{pmatrix}. \quad (\text{A1c})$$

Each of these operators satisfies

$$R_a(\beta)R_a(\alpha) = R_a(\alpha + \beta), \quad a = x, y, z, \quad (\text{A2})$$

and the same applies to

$$P(\theta) = \begin{pmatrix} 1 & 0 \\ 0 & e^{i\theta} \end{pmatrix}. \quad (\text{A3})$$

The rotation

$$R_c(v) = R_y(\theta_{v,2})R_z(\theta_{v,1}), \quad (\text{A4})$$

can be used to compute a complex value, $v = |v| \exp(i \arg(v))$, by acting on the zero state:

$$R_c(v) |0\rangle = \cos(\theta_{v,2}/2) e^{-i\theta_{v,1}/2} |0\rangle + \sin(\theta_{v,2}/2) e^{-i\theta_{v,1}/2} |1\rangle, \quad (\text{A5})$$

where v can be encoded as a complex amplitude of either the zero state, $v = \cos(\theta_{v,2}/2) e^{-i\theta_{v,1}/2}$, or the unit state, $v = \sin(\theta_{v,2}/2) e^{-i\theta_{v,1}/2}$.

2. Parameters for the oracle O_H

The rotations from Sec. A 1 are used in the oracle O_H (Figs. 6 and 7) with the following angles:

$$\theta_{\omega, \varepsilon_L} = 2 \arcsin(-\omega \varepsilon_L d_H), \quad L \in [0, 1], \quad (\text{A6a})$$

$$\theta_{\omega} = 2 \arcsin(-\omega d_H), \quad (\text{A6b})$$

$$\theta_{\omega, \varepsilon_0, e} = 2 \arcsin(-\omega \varepsilon_0 d_H^{3/2}), \quad (\text{A6c})$$

$$\theta_{\omega, e} = 2 \arcsin(-\omega d_H^{3/2}), \quad (\text{A6d})$$

$$\theta_{\eta_{\pm, 1}} = -2 \arg(\eta_{\pm}), \quad (\text{A6e})$$

$$\theta_{\eta_{+, 2}} = 2 \arcsin(|\eta_+| d_H^{3/2}), \quad (\text{A6f})$$

$$\theta_{\eta_{-, 2}} = 2 \arcsin(|\eta_-| d_H^{3/2}), \quad (\text{A6g})$$

$$\theta_{\pm \sigma} = 2 \arcsin(\pm \sigma d_H^2), \quad (\text{A6h})$$

$$\theta_{\pm \sigma, e} = 2 \arcsin(\pm \sigma d_H^{3/2}) - \theta_{\pm \sigma}, \quad (\text{A6i})$$

$$\theta_{\pm \pi} = -\theta_{\pm \sigma}. \quad (\text{A6j})$$

For instance, the angles $\theta_{\omega, \varepsilon_0}$ are used in the oracle $O_{H, \omega}$ shown in Fig. 7 to compute the elements $i\omega \varepsilon_0$ of the matrix (43) at the rows with $k \in [2, 2N_x - 3]$. According to Eq. (54), for these elements, the oracle O_S returns the multiplication factor d_H^{-1} , which is taken into account in Eq. (A6a). The elements $i\omega \varepsilon_0$ also appear at $k = 1$ and $k = N_x - 2$ in the matrix (43). However, for these indices, the oracle O_S returns $d_H^{-3/2}$ that is taken into account in the computation of the angle $\theta_{\omega, \varepsilon_0, e}$, where the subindex “e” stands for “edge” (boundary). The same principle applies to the calculation of the angles θ_{ω} and $\theta_{\omega, e}$, also $\theta_{\pm \sigma}$ and $\theta_{\pm \sigma, e}$.

3. Arithmetic operators

Apart from the incrementor and decrementor used in Fig. 5 and described in Ref. [4], we use also a subtractor $S_{k_{\text{sub}}}$ and a comparator $C_{k_{\text{com}}}$. The former operator (Fig. 17) subtracts the predefined unsigned integer k_{sub} from the integer(s) encoded in the n_t target qubits t . Its implementation is based on the circuit described in Ref. [56]. In our realization, the most significant (the uppermost) qubit is used to store the sign of the resulting integer, and the absolute value of the output integer is written back to the target qubits.

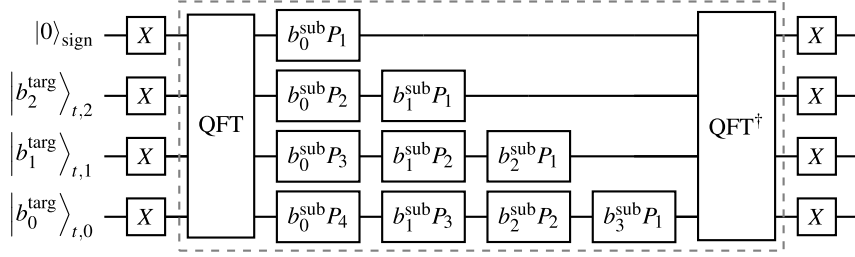


FIG. 17. The circuit for the subtractor $S_{k_{\text{sub}}}$ for the case with $n_t = 3$ target qubits, where the unsigned integer k_{sub} is represented as the bit string $[b_3^{\text{sub}} b_2^{\text{sub}} b_1^{\text{sub}} b_0^{\text{sub}}]$ (b_0^{sub} is the least significant bit). The operator subtracts k_{sub} from the unsigned integer, k_{targ} , encoded as the bit string $|b_2^{\text{targ}} b_1^{\text{targ}} b_0^{\text{targ}}\rangle_t$ into the target register t . The difference $\Delta = k_{\text{targ}} - k_{\text{sub}}$ is written back to the register t , and the “sign” qubit is inverted if the result is negative. Here, $b_j^{\text{sub}} P_k$ applies the phase gate $P(2\pi/2^k)$ [Eq. (A3)] if $b_j^{\text{sub}} = 1$. The inner dashed box is the adder, $k_{\text{targ}} + k_{\text{sub}}$, where the “sign” qubit stores the carry bit of the sum.

By removing the X gates from Fig. 17, one obtains the adder $A_{k_{\text{sub}}}$ that adds the integer k_{sub} to the integer(s) encoded in the register t .

The subtractor is used to construct the comparator [56] $C_{k_{\text{com}}}$ that inverts the “com” ancilla qubit (Fig. 16) if the predefined unsigned integer k_{com} is strictly larger than the integer encoded in the target qubits. The comparator leaves the target qubits and the “sign” qubit (used for the intermediate computations within the comparator) untouched. More details can be found in Ref. [56]. (Keep in mind that the least significant qubit in all our circuits is the lowermost one.)

As shown in Ref. [57], the circuit presented in Fig. 17 can be modified to subtract the integer k_{sub} , which is not predefined but encoded as a bit string in another register r_{sub} . For that, the phase gates P_k in the subtractor should be controlled by the corresponding qubits of the register r_{sub} . This operator acts then on two registers, t and r_{sub} , and is denoted here as $S_{t-r_{\text{sub}}}$. The resulting difference is written back to the target register t .

The circuits for the subtractors and the comparator require $\mathcal{O}(n^2)$ quantum operations.

APPENDIX B: QSVT COMPUTATION OF A GAUSSIAN FUNCTION

1. General algorithm

To calculate the absolute value of the absorption power given by Eq. (70), one needs to compute the Gaussian function G in the quantum circuit. This function can be approximated by a polynomial by using the Fourier approach, Eq. (17). The circuit for the polynomial is constructed by using the QSVT (Fig. 1). The QSVT finds the polynomial as a function of singular values of some given matrix M . If the matrix is diagonal, and the spatial coordinate grid is placed at the diagonal, $M = \text{diag}(x)$, then the QSVT computes the polynomial of the coordinate x . After that, M is block encoded into the unitary matrix U_A , which

is used within the QSVT circuit as shown in Fig. 1. However, since the x grid, x_j , is a linear function of the index j , it is problematic to encode the x points directly into U_A by using quantum gates, which are more naturally suited to represent rotations. Instead, one can encode $\psi = \sin(x)$ and consider the Gaussian as a function of $\arcsin(\psi)$:

$$G(\psi) = \beta_{\text{sc}} \exp\left(-\frac{\arcsin^2(\psi)}{2\mu^2}\right), \quad (\text{B1})$$

where β_{sc} is a rescaling factor, μ is the Gaussian width. To block encode $\psi_j = \sin(x_j)$, the circuit shown in Fig. 18 is used. This circuit generates the sine of x_j :

$$x_j = \alpha_0 + j \Delta x, \quad j = [0, N_x), \quad \Delta x = 2\alpha/N_x. \quad (\text{B2})$$

Similar to Sec. IV B, we have $N_x = 2^{n_x}$, and the register r_x in Fig. 18 has n_x qubits. For the given integer j encoded as a bit string in the register r_x , the circuit returns $\sin(x_j)$ as the amplitude of the zero state of the ancilla a . It can be shown using Eq. (A1b) that the x grid from $-1.0 - x_c$ to $1.0 - x_c$ for some real x_c is generated by the following parameters:

$$\alpha_0 = -1.0 - x_c, \quad \alpha = N_x/(N_x - 1). \quad (\text{B3})$$

The Gaussian generated on this grid is centered at x_c (Fig. 19).

The Gaussian (B1) is approximated by a polynomial of definite parity by using the Fourier approach (17), and the QSVT angles are computed by using the minimization procedure [22]. [By setting $\beta_{\text{sc}} < 1$ in Eq. (B1), one can speed up the calculation of the QSVT angles.] Since the Gaussian is an even function, the resulting QSVT circuit does not include the last three operators indicated by the dashed box in Fig. 1. The QSVT circuit uses the oracle U_A shown in Fig. 18 to encode $\psi(x)$. As shown in Fig. 19, the number of the QSVT angles depends logarithmically on

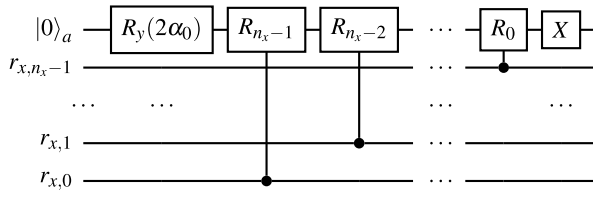


FIG. 18. The circuit implementing the matrix U_A for the encoding of the coordinate $\psi = \sin(x)$ according to Eqs. (B2). Here, $R_k = R_y(2\alpha/2^k)$.

$\varepsilon_{\text{QSVT}}$ for small μ , and the dependence becomes polynomial for $\mu \gtrsim 0.25$ (Fig. 19). If the Gaussian peak is narrow ($\mu < 0.05$) or becomes comparable with the length of the spatial domain $x = [-1.0, 1.0]$ ($\mu > 0.25$), the number of angles grows exponentially with μ for a fixed $\varepsilon_{\text{QSVT}}$.

2. Two Gaussians

To demonstrate this technique, we construct two Gaussians by using the QSVT and integrate them in space by using AE. This is an illustration of the “parallel” computation in quantum circuits: by applying the QSVT circuit only once, we construct two Gauss functions at the same time. The corresponding circuit is shown in Fig. 20, where the x grid is prepared by creating a uniform superposition of states in the register r_x and using the parameters from Eqs. (B3). The QSVT circuit is applied only to the first $n_x - 1$ qubits of the register r_x . Since the last qubit (the most significant one) is in the superposition $(|0\rangle + |1\rangle)/\sqrt{2}$, the QSVT entangles one Gaussian with the zero state of this qubit and another Gaussian with the unit state:

$$|\psi_G\rangle = 2^{-n_x/2} (|0\rangle_{r_x, n_x-1} |G(x)\rangle_{r_x, [0, n_x-2]} + |1\rangle_{r_x, n_x-1} |G(x)\rangle_{r_x, [0, n_x-2]}), \quad (\text{B4})$$

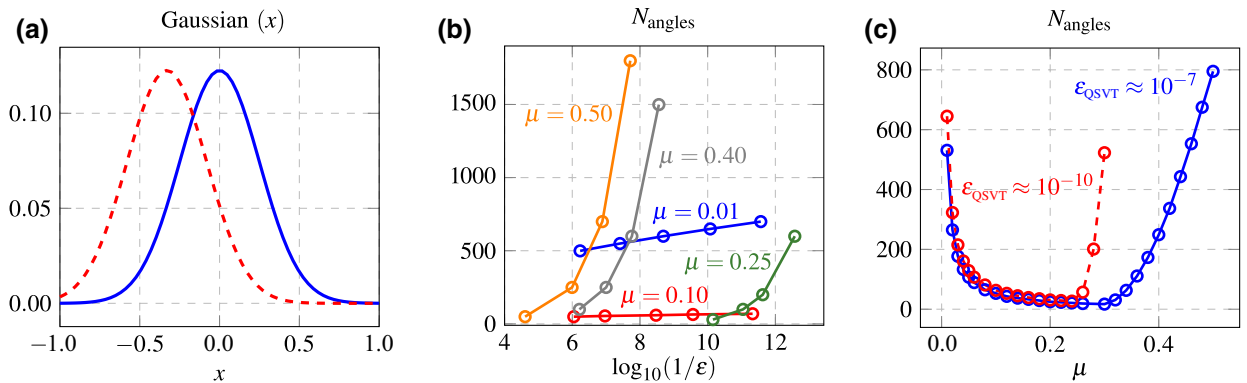


FIG. 19. (a) The Gaussian functions computed by the QSVT and centered around $x_c = 0.0$ (solid blue line) and $x_c = -0.33$ (dashed red line). Here, $\beta_{\text{sc}} = 0.98$, $\mu = 0.25$, and $n_x = 6$. The peak amplitude is downscaled by the factor $2^{n_x/2}$ due to the initialization, which is the same as in the circuit shown in Fig. 20. (b) The dependence of the number of the QSVT angles, N_{angles} , on the QSVT approximation error $\varepsilon_{\text{QSVT}}$ for various widths μ . (c) The dependence of N_{angles} on μ for $\varepsilon_{\text{QSVT}} = 10^{-7}$ and $\varepsilon_{\text{QSVT}} = 10^{-10}$.

where the state $|\psi_G\rangle$ is indicated in Fig. 20. The most significant qubit in r_x encodes the left spatial domain, $x < 0$, if the qubit is in the zero state, and the right spatial domain, $x > 0$, if the qubit is in the unit state. Therefore, the superposition (B4) corresponds to one Gaussian in the domain $x = [-1.0, 0.0]$ and another Gaussian in $x = (0.0, 1.0]$ as shown in Fig. 21. Apart from that, if the original Gaussian is defined according to Eq. (B1), then the resulting Gaussians have widths $\mu/2$. Also, due to the initialization circuit (green box in Fig. 20), the Gaussians are multiplied by the factor $\beta_{\text{init}} = 2^{-n_x/2}$.

The circuit shown in Fig. 20 integrates the Gaussians in the second and third quarters of the spatial domain:

$$S_G = p_{m,1}/N_x, \quad (\text{B5a})$$

$$p_{m,1} = \beta_{\text{init}}^2 \sum_{x=(-0.5, 0.5)} |G(x)|^2. \quad (\text{B5b})$$

The quantum state encoding the desired spatial interval is entangled with $|1\rangle_m$, and then $p_{m,1}$ is computed by using the AE. As explained in Sec. VI C, the AE consists of several queries to the AA operator. In our case, the latter is defined as

$$\text{AA} = U_{\text{prep}} \text{REF}_0 U_{\text{prep}}^\dagger \text{REF}_G, \quad (\text{B6})$$

where U_{prep} is marked in Fig. 20 with the black dashed box, REF_0 is the reflector around the initial (in our case, zero) state, REF_G is the reflector around the state of interest produced by U_{prep} . Here, the state of interest is $|1\rangle_m$, thus, REF_G is represented by a single Pauli-Z gate at the qubit m . The reflector REF_0 is constructed as the sequence $XZZX$ at the qubit m controlled by the zero states of the registers r_x , a , q , and “sum.”

The whole circuit shown in Fig. 20 is computed on an emulator of quantum computers [27]. The AE of S_G is

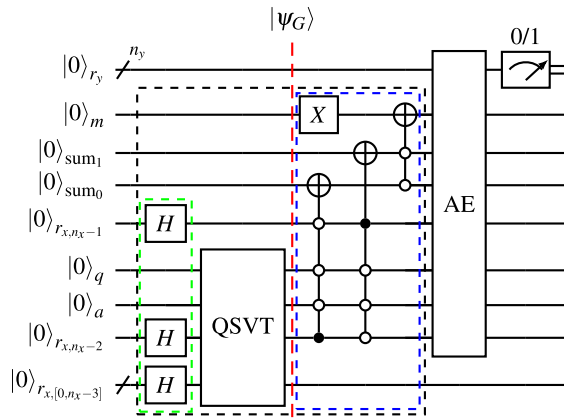


FIG. 20. The circuit for the construction of one Gaussian in the left spatial domain ($x < 0$) and another Gaussian in the right domain ($x > 0$) as shown in Fig. 21. The circuit also integrates the function in the second and third quarters of the spatial area, $x = (-0.5, 0.5)$. The QSVT circuit uses the subcircuit presented in Fig. 18 as the block-encoding oracle. The green box indicates the initialization subcircuit. The blue box entangles the unit state $|1\rangle_m$ with the spatial distribution of the Gaussians in $x = (-0.5, 0.5)$ by using the ancilla register “sum.” The most significant qubit of the register r_x is separated from the rest of the register qubits to show correctly the location of the QSVT subcircuit. The black dashed box indicates the circuit U_{prep} .

shown in Fig. 21 and compared with the value computed classically.

3. Gaussian as a filter

The Gaussian constructed by the QSVT can be used as a filter in real or Fourier space. In particular, to calculate

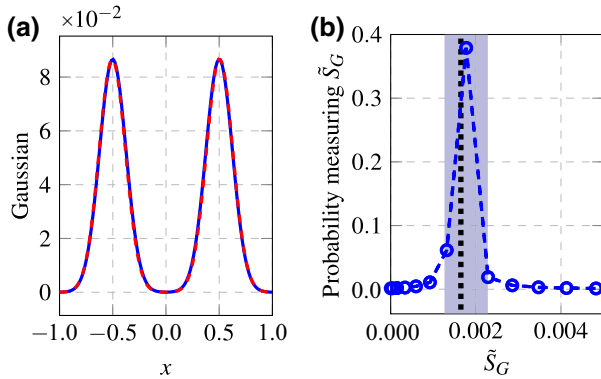


FIG. 21. (a) Two Gaussians encoded in the intermediate state $|\psi_G\rangle$ produced in the circuit shown in Fig. 20 (red dashed line) and computed classically (solid blue line). Here, $\mu = 0.250$ is used in Eq. (B1), and the resulting width of each Gaussian is $\mu = 0.125$. (b) Probability distribution of measurement results \tilde{S}_G from the circuit shown in Fig. 20, where $n_y = 6$. The shaded area marks the interval where the analytical error is bounded as described in Eq. (63). The vertical black dotted line corresponds to S_G computed classically using Eq. (B5).

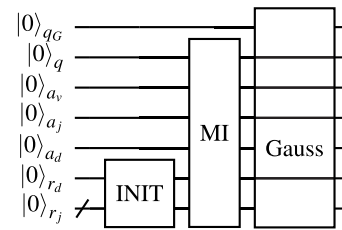


FIG. 22. The circuit for the computation of the product $G(x)F(x)$, where $G(x)$ is the Gaussian modeled by the QSVT subcircuit “Gauss,” $F(x)$ is the field, electric or magnetic, simulated by the QSVT subcircuit “MI.” The qubits that pass above the circuit “Gauss” are not used by it. The initialization “INIT” is the same as discussed in Sec. VB.

the product of the EM fields $F(x)$ with the Gaussian, $G(x)F(x)$, one can use the circuit shown in Fig. 22. Here, the main question is whether it is possible to use the same ancillae in the QSVT for the computation of $F(x)$ (the “MI” subcircuit) and in the QSVT for the Gaussian calculation (the “Gauss” subcircuit). The computation shows that one does not need to control the “Gauss” by the zero states of the ancillae used in the “MI” (i.e., ancilla registers q, a_v, a_j), and the same ancilla a_d can be used in both QSVT subcircuits. However, for the Gaussian QSVT, it is necessary to introduce another ancilla q_G equivalent to the ancilla q in the “MI.”

Since the “Gauss” subcircuit is not controlled by the qubit r_d , which is responsible for the choice between the electric and magnetic fields, the circuit constructs the product $G(x)F(x)$ for both fields in parallel. The circuit shown in Fig. 22 outputs the spatial distribution $G(x)E(x)$ (entangled with $|0\rangle_{r_d}$) and $G(x)B(x)$ (entangled with $|1\rangle_{r_d}$) if all ancillae are in the zero state. The signals $G(x)F(x)$ obtained from the emulation of this circuit are shown in Fig. 23 and compared with classical simulations.

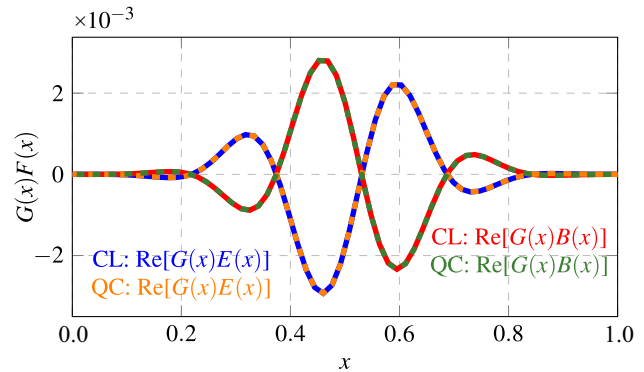


FIG. 23. The product of the Gaussian G with electromagnetic fields simulated classically (CL, solid lines) and by using the circuit shown in Fig. 22 (QC, dashed lines).

- [1] N. J. Fisch, Theory of current drive in plasmas, *Rev. Mod. Phys.* **59**, 175 (1987).
- [2] R. I. Pinsker, Introduction to wave heating and current drive in magnetized plasmas, *Phys. Plasmas* **8**, 1219 (2001).
- [3] R. Prater, Heating and current drive by electron cyclotron waves, *Phys. Plasmas* **11**, 2349 (2004).
- [4] I. Novikau, E. A. Startsev, and I. Y. Dodin, Quantum signal processing for simulating cold plasma waves, *Phys. Rev. A* **105**, 062444 (2022).
- [5] A. Engel, G. Smith, and S. E. Parker, Quantum algorithm for the Vlasov equation, *Phys. Rev. A* **100**, 062315 (2019).
- [6] V. Lancellotti, D. Milanese, R. Maggiora, G. Vecchi, and V. Korytsya, TOPICA: an accurate and efficient numerical tool for analysis and design of ICRF antennas, *Nucl. Fusion* **46**, S476 (2006).
- [7] S. Shiraiwa, J. C. Wright, P. T. Bonoli, T. Kolev, and M. Stowell, RF wave simulation for cold edge plasmas using the MFEM library, *EPJ Web Conf.* **157**, 03048 (2017).
- [8] V. A. Svidzinski, J. S. Kim, L. Zhao, S. A. Galkin, and J. A. Spencer, Hybrid iterative approach for simulation of radio-frequency fields in plasma, *Phys. Plasmas* **25**, 082509 (2018).
- [9] J. Hillairet, WEST actively cooled load resilient ion cyclotron resonance heating system results, *Nucl. Fusion* **61**, 096030 (2021).
- [10] W. Zhang, R. Bilato, V. Bobkov, A. Cathey, A. D. Siena, M. Hoelzl, A. Messiaen, J. Myra, G. S. López, W. Tierens, M. Usoltceva, J. Wright, the ASDEX Upgrade Team, the EUROfusion MST1 Team, Recent progress in modeling ICRF-edge plasma interactions with application to ASDEX upgrade, *Nucl. Fusion* **62**, 075001 (2022).
- [11] W. Guttenfelder, NSTX-U theory, modeling and analysis results, *Nucl. Fusion* **62**, 042023 (2022).
- [12] I. Y. Dodin and E. A. Startsev, On applications of quantum computing to plasma simulations, *Phys. Plasmas* **28**, 092101 (2021).
- [13] A. W. Harrow, A. Hassidim, and S. Lloyd, Quantum Algorithm for Linear Systems of Equations, *Phys. Rev. Lett.* **103**, 150502 (2009).
- [14] A. Ambainis, in *29th International Symposium on Theoretical Aspects of Computer Science (STACS 2012)*, edited by C. Dürr, T. Wilke (Eds.), Leibniz International Proceedings in Informatics (LIPIcs), Vol. 14 (Schloss Dagstuhl–Leibniz-Zentrum fuer Informatik, Dagstuhl, Germany, 2012), pp. 636–647, <http://drops.dagstuhl.de/opus/volltexte/2012/3426>.
- [15] A. M. Childs, R. Kothari, and R. D. Somma, Quantum algorithm for systems of linear equations with exponentially improved dependence on precision, *SIAM J. Comput.* **46**, 1920 (2017).
- [16] A. Scherer, B. Valiron, S.-C. Mau, S. Alexander, E. van den Berg, and T. E. Chapuran, Concrete resource analysis of the quantum linear-system algorithm used to compute the electromagnetic scattering cross section of a 2D target, *Quantum Inf. Process.* **16**, 1 (2017).
- [17] G. H. Low and I. L. Chuang, Optimal Hamiltonian Simulation by Quantum Signal Processing, *Phys. Rev. Lett.* **118**, 010501 (2017).
- [18] G. H. Low and I. L. Chuang, Hamiltonian simulation by qubitization, *Quantum* **3**, 163 (2019).
- [19] A. Gilyén, Y. Su, G. H. Low, and N. Wiebe, in *Proceedings of the 51st Annual ACM SIGACT Symposium on Theory of Computing, STOC 2019* (Association for Computing Machinery, New York, NY, USA, 2019), p. 193–204, <https://doi.org/10.1145/3313276.3316366>.
- [20] J. M. Martyn, Z. M. Rossi, A. K. Tan, and I. L. Chuang, Grand Unification of Quantum Algorithms, *PRX Quantum* **2**, 040203 (2021).
- [21] A. Montanaro and S. Pallister, Quantum algorithms and the finite element method, *Phys. Rev. A* **93**, 032324 (2016).
- [22] Y. Dong, X. Meng, K. B. Whaley, and L. Lin, Efficient phase-factor evaluation in quantum signal processing, *Phys. Rev. A* **103**, 042419 (2021).
- [23] L. Lin, <https://arxiv.org/abs/2201.08309>.
- [24] W. H. Press, S. A. Teukolsky, W. T. Vetterling, and B. P. Flannery, *Numerical Recipes 3rd Edition: The Art of Scientific Computing* (Cambridge University Press, USA, 2007), 3rd ed.
- [25] E. Remez, Sur la détermination des polynômes d'approximation de degré donnée, *Commun. Soc. Math. Kharkov* **10**, 41 (1934).
- [26] Efficient phase-factor evaluation in quantum signal processing: Code (2022), <https://github.com/qsppack/QSPACK>.
- [27] Numerical QSP framework implemented in C++ with the application of QuEST library (2022), https://github.com/ivanNovikau/QSVT_framework.
- [28] J. Haah, Product decomposition of periodic functions in quantum signal processing, *Quantum* **3**, 190 (2019).
- [29] Computation of angles for quantum signal processing in F# (2020), <https://github.com/microsoft/Quantum-NC/tree/main/src/simulation/qsppack>.
- [30] L. Ying, <https://arxiv.org/abs/2202.02671>.
- [31] R. E. Bank and L. R. Scott, On the conditioning of finite element equations with highly refined meshes, *SIAM J. Numer. Anal.* **26**, 1383 (1989).
- [32] Y. Saad, *Iterative Methods for Sparse Linear Systems* (Society for Industrial and Applied Mathematics, Philadelphia, 2003).
- [33] H. A. van der Vorst, Bi-CGSTAB: A fast and smoothly converging variant of BI-CG for the solution of nonsymmetric linear systems, *SIAM J. Sci. Stat. Comput.* **13**, 631 (1992).
- [34] Y. Saad and M. H. Schultz, GMRES: A generalized minimal residual algorithm for solving nonsymmetric linear systems, *SIAM J. Sci. Stat. Comput.* **7**, 856 (1986).
- [35] R. W. Freund, A transpose-free quasi-minimal residual algorithm for non-Hermitian linear systems, *SIAM J. Sci. Comput.* **14**, 470 (1993).
- [36] J. R. Shewchuk, Technical Report No. CMU-CS-94-125, an introduction to the conjugate gradient method without the agonizing pain, Tech. Rep. (Carnegie Mellon University, Pittsburgh, Pennsylvania, USA, 1994), <https://dl.acm.org/doi/10.5555/865018>.
- [37] B. D. Clader, B. C. Jacobs, and C. R. Sprouse, Preconditioned Quantum Linear System Algorithm, *Phys. Rev. Lett.* **110**, 250504 (2013).

- [38] G. Vahala, L. Vahala, M. Soe, and A. K. Ram, Unitary quantum lattice simulations for Maxwell equations in vacuum and in dielectric media, *J. Plasma Phys.* **86**, 905860518 (2020).
- [39] A. K. Ram, G. Vahala, L. Vahala, and M. Soe, Reflection and transmission of electromagnetic pulses at a planar dielectric interface: Theory and quantum lattice simulations, *AIP Adv.* **11**, 105116 (2021).
- [40] G. Vahala, M. Soe, L. Vahala, and A. K. Ram, One- and two-dimensional quantum lattice algorithms for Maxwell equations in inhomogeneous scalar dielectric media. II: Simulations, *Radiat. Eff. Defects Solids* **176**, 64 (2021).
- [41] E. Koukoutsis, K. Hizanidis, A. K. Ram, and G. Vahala, <https://arxiv.org/abs/2209.08523>.
- [42] S. Jin, N. Liu, and Y. Yu, Time complexity analysis of quantum difference methods for linear high dimensional and multiscale partial differential equations, *J. Comput. Phys.* **471**, 111641 (2022).
- [43] D. W. Berry and A. M. Childs, Black-box Hamiltonian simulation and unitary implementation, *Quantum Info. Comput.* **12**, 29 (2012).
- [44] A. Barenco, C. H. Bennett, R. Cleve, D. P. DiVincenzo, N. Margolus, P. Shor, T. Sleator, J. A. Smolin, and H. Weinfurter, Elementary gates for quantum computation, *Phys. Rev. A* **52**, 3457 (1995).
- [45] T. Jones, A. Brown, I. Bush, and S. C. Benjamin, Quest and high performance simulation of quantum computers, *Sci. Rep.* **9**, 10736 (2019).
- [46] M. A. Nielsen and I. L. Chuang, *Quantum Computation and Quantum Information* (Cambridge University Press, New York, 2010), 10th Anniversary edition.
- [47] G. Brassard, P. Høyer, M. Mosca, and A. Tapp, Quantum amplitude amplification and estimation, *Quantum Comput. Inf.* **305**, 53 (2002).
- [48] T. H. Stix, *Waves in Plasmas* (AIP Press, New York, 1992).
- [49] E. R. Tracy, A. J. Brizard, A. S. Richardson, and A. N. Kaufman, *Ray Tracing and Beyond: Phase Space Methods in Plasma Wave Theory* (Cambridge University Press, New York, 2014).
- [50] D. Grinko, J. Gacon, C. Zoufal, and S. Woerner, Iterative quantum amplitude estimation, *npj Quantum Inf.* **7**, 52 (2021).
- [51] V. A. Svidzinski, J. S. Kim, J. A. Spencer, L. Zhao, S. A. Galkin, and E. G. Evstatiev, Hot plasma dielectric response to radio-frequency fields in inhomogeneous magnetic field, *Phys. Plasmas* **23**, 112101 (2016).
- [52] G. Ortiz, J. E. Gubernatis, E. Knill, and R. Laflamme, Quantum algorithms for fermionic simulations, *Phys. Rev. A* **64**, 022319 (2001).
- [53] K. Mitarai and K. Fujii, Methodology for replacing indirect measurements with direct measurements, *Phys. Rev. Res.* **1**, 013006 (2019).
- [54] H. Buhrman, R. Cleve, J. Watrous, and R. de Wolf, Quantum Fingerprinting, *Phys. Rev. Lett.* **87**, 167902 (2001).
- [55] D. L. Green, E. D’Azevedo, D. B. Batchelor, N. Bertelli, C. Lau, R. L. Barnett, and J. F. C. Marin, A WKB based preconditioner for the 1D Helmholtz wave equation, *AIP Conf. Proc.* **2254**, 060008 (2020).
- [56] A. Suau, G. Staffelbach, and H. Calandra, Practical quantum computing, *ACM Trans. Quantum Comput.* **2**, 1 (2021).
- [57] T. G. Draper, <https://arxiv.org/abs/quant-ph/0008033>.